

Intraflagellar transport complex B proteins regulate the Hippo effector Yap1 during cardiogenesis

Marina Peralta^{1,2,3,4}, Katerina Jerabkova^{1,2,3,4*}, Tommaso Lucchesi^{5,6,7*}, Laia Ortiz Lopez^{1,2,3,4}, Benjamin Vitre⁸, Dong Han^{5,6}, Laurent Guillemot^{5,6}, Chaitanya Dingare⁹, Izabela Sumara^{1,2,3,4}, Nadia Mercader^{10,11}, Virginie Lecaudey⁹, Benedicte Delaval⁸, Sigolène M. Meilhac^{5,6} and Julien Vermot^{1,2,3,4}

¹Institut de Génétique et de Biologie Moléculaire et Cellulaire, Illkirch, France

²Centre National de la Recherche Scientifique, UMR7104, Illkirch, France

³Institut National de la Santé et de la Recherche Médicale, U964, Illkirch, France

⁴Université de Strasbourg, Illkirch, France

⁵*Imagine* - Institut Pasteur, Laboratory of Heart Morphogenesis, Paris, France

⁶INSERM UMR1163, Université Paris Descartes, Paris, France

⁷Sorbonne Université, Collège Doctoral, F-75005, Paris, France

⁸Centre de Recherche en Biologie cellulaire de Montpellier, (CRBM), CNRS, Univ. Montpellier, Montpellier, France

⁹Institute for Cell Biology and Neurosciences, Goethe University of Frankfurt, Germany

¹⁰Institute of Anatomy, University of Bern, Switzerland

¹¹Centro Nacional de Investigaciones Cardiovasculares CNIC, Madrid, Spain

*equal second authors listed in alphabetical order.

Abstract

Cilia and the intraflagellar transport (IFT) proteins involved in ciliogenesis are associated with congenital heart diseases (CHD). However, the molecular links between cilia, IFT proteins and cardiogenesis are yet to be established. Using a combination of biochemistry, genetics, and live imaging methods, we show that IFT complex B proteins (Ift88, Ift54 and Ift20) modulate the Hippo pathway effector YAP1 in zebrafish and mouse. We demonstrate that this interaction is key to restrict the formation of the proepicardium and the myocardium. *In cellulo* experiments suggest that IFT88 and IFT20 interact with YAP1 in the cytoplasm and functionally modulates its activity, identifying a molecular link between cilia related proteins and the Hippo pathway. Taken together, our results highlight a novel role for IFT complex B proteins during cardiogenesis and shed light on an unexpected mechanism of action for ciliary proteins in YAP1 regulation. These findings provide mechanistic insights into a non-canonical role for cilia related proteins during cardiogenesis.

Introduction

Primary cilia are immotile microtubule-based organelles, well known for being both chemical and/or mechanical sensors (1). Disruption of cilia function causes multiple human syndromes known as ciliopathies (2). Cilia are required for cardiac development and mutations in cilia-related proteins have been linked to congenital heart diseases (CHDs) (3–6). Nevertheless, the specific role of cilia and cilia-related proteins during cardiogenesis is still unclear.

Intraflagellar transport (IFT) proteins are required for the transport of cilia components along the axoneme and are thus essential for cilia formation and function (7). The role of IFT proteins during ciliogenesis is highly conserved across organisms (8). The IFT machinery is composed of two biochemically distinct subcomplexes, IFT-A and IFT-B (8). The IFT complex B member IFT20, which localizes inside the cilium and at the Golgi complex in mammalian cells, participates in the sorting and/or transport of membrane proteins for the cilia (9). Within the IFT complex B, IFT20 interacts with IFT54/Elipsa (10,11), and IFT88 which is essential for flagellar assembly in *Chlamydomonas* and ciliogenesis in vertebrates (12). Mutations in IFT proteins lead to ciliary defects and to several ciliopathies (2). Importantly, some IFT proteins have been identified in CHDs(4). IFT proteins also display non-canonical, cilia-independent functions (13,14). IFT88, for example, is needed for spindle orientation or cleavage furrow ingression in dividing cells (15,16) and regulates G1-S phase transition in non-ciliated cells (17). IFT20, together with IFT88 and IFT54, plays a role in the establishment of the immune synapse in T-lymphocytes lacking cilia (18,19). These observations suggest that IFT proteins could play a key role in embryonic cardiogenesis through both cilia-dependent and – independent functions.

The Hippo signaling mediators, YAP1/WWTR1 (TAZ), constitute a key signaling pathway for the regulation of cardiac development (20–23) and cardiac regeneration (24,25) in vertebrates. For example, YAP1/WWTR1 (TAZ) are required for epicardium and coronary vasculature development (26) in mice. Changes in cell shape, substrate stiffness and tension forces activate a phosphorylation-independent YAP1/WWTR1 (TAZ) modulation (27) which is mediated by the Motin family (AMOT, AMOTL1, and AMOTL2) (28,29). Motin proteins bind to YAP/WWTR1 (TAZ) sequestering them in the cytoplasm in several cellular contexts (30–34). While it is known that ciliary proteins from the Nephrocystin family modulate the transcriptional activity of YAP1/WWTR1 (TAZ) (35–37) and that the Hippo kinases MST1/2-

SAV1 pathway promotes ciliogenesis (38), the connection between the Hippo pathway and cilia function remains unclear.

Cardiogenesis involves an interplay between multiple tissue layers. The epicardium is the outermost layer covering the heart. This cardiac cell layer plays an essential role in myocardial maturation and coronary vessel formation during development (39–41) and has a crucial role during regeneration (42–44). Epicardial cells derive from the proepicardium (PE), an extra-cardiac transient cluster of heterogeneous cells (45). In mice, the PE is a single cell cluster located close to the venous pole of the heart (45), while in zebrafish is composed by two cell clusters, avcPE (the main source of cells) and vpPE (46). Proepicardial cells give rise to the epicardium, part of the coronary vasculature and intracardiac fibroblasts (45,47–49). The secreted signaling molecules of the bone morphogenetic protein (BMP) family are indispensable for PE formation (50–52). However, the regulation of PE development remains poorly understood.

Despite the increasing evidence for the role of IFT proteins in cell signaling, it has been difficult to pinpoint the exact function of cilia-related proteins outside the cilium. Without this key information, the question of whether cilia-related proteins can affect the developmental program independently of their cilia function remains unresolved. Here, we provide a combination of *in vivo* and *in vitro* analyses of IFT protein function showing that IFT complex B proteins can modulate the Hippo pathway effector Yap1. In particular, we show that IFT88 is required to restrict proepicardial and myocardial development through cytoplasmic activity.

Results

IFT complex B proteins regulate proepicardial development in zebrafish and mouse.

Considering the importance of cilia during cardiogenesis, we assessed the role of several IFT complex B proteins during embryonic cardiogenesis *in vivo* focusing on the PE. In order to

benefit from live imaging and genetics, we used zebrafish as a model organism. We performed live imaging focusing on the main PE cell source located near the atrioventricular canal (avcPE) in *ift88* (53) and *elipsa/ift54* (10) mutants (**Fig. 1 A-D**) (**Supp. 1 B, C**). Between 50 hpf and 57 hpf, we found that *ift88* mutants display multiple avcPE clusters (either 2 or 3), when controls have only one (**Movie 1**). Using a *wilms tumor 1 a* (*wt1a*) enhancer trap line that marks proepicardial and epicardial cells (*Et(-26.5Hsa.WT1-gata2:EGFP)^{cnl}* hereafter *epi:GFP*) (46) we quantified avcPE and epicardial cell number and found that *ift88*^{-/-} have increased avcPE cell numbers compared to their controls at 50 hpf. We additionally found that the size change is associated with an increased number of epicardial cells number in *ift88*^{-/-} embryos (**Supp. 2 A**). Similarly, we found that *elipsa*^{-/-} also showed bigger avcPE compared to controls (**Fig. 1 D**) (**Supp. 1 A''**). Taken together, these data indicate that *ift88* and *elipsa/ift54* are required to restrict PE size.

To determine whether primary cilia are required for PE formation, we took advantage of the *iguana/dzip* (54) mutant, a well-established cilia mutant lacking primary cilia (55). We confirmed the absence of primary cilia in the pericardial cavity of the *iguana*^{-/-} using the cilia reporter *actb2:Mmu.Arl13b-GFP* (56) (**Supp. 2 C-E**) (**Movie 2**). Zebrafish *ift* genes are expressed maternally (57) (**Supp. 2 E**) and complete removal of both zygotic and maternal expression of *ift88* leads to the ablation of primary cilia resembling the *iguana* mutant phenotype (58). Live imaging revealed that a significant fraction of *iguana* mutants lacked an avcPE between 50 hpf and 57 hpf (**Fig. 1 B**) (**Movie 3**). At 55 hpf, *iguana*^{-/-} displayed decreased avcPE cell numbers (**Fig. 1 D**) (**Supp. 1 A and 2 A'**). Since the *iguana* mutants presented a phenotype opposite to that of the *ift88* mutants, we analyzed the *ift88*^{-/-}; *iguana*^{-/-}; *epi:GFP* double mutant to elucidate whether the differences could be due to a new cilia-independent function. The *ift88*^{-/-}; *iguana*^{-/-} double mutant shows multiple avcPE cluster formation and an

increased avcPE cell number, reminiscent of *ift88* loss of function (**Fig. 1 E, F**) (**Supp. 1 D**).

We conclude that *Ift88* modulates the PE cell number independently of its cilia function.

We next assessed whether the role of IFT complex B proteins during PE formation was conserved in mammals. We analyzed the PE in *Ift20* and *Ift88* knock-out (KO) mice at mouse embryonic day (E) 9.5 (**Fig. 1 G, H**) (**Supp. 3 A, B**). First, we performed immunofluorescence using an anti-Arl13b antibody to quantify the percentage of ciliated PE cells in *Ift20*, *Ift88 KO* and *wild type* mice (**Supp. 3 C-C''**). We found that, while over 60% of the *wild type* PE cells were ciliated, in *Ift88 KO* mice only 3% of PE cells were ciliated and *Ift20 KO* embryos lack cilia (**Supp. 3 C''**). We compared the PE volume of *Ift20 KO* mice to their controls, using an anti-Wt1 antibody (a well-established PE marker (59)). Mutant embryos showed increased PE volume compared to controls (**Movie 5, 6**). Likewise, the PE volume in *Ift88 KO* was also increased compared to controls (**Fig. 1 H**). Together, these results suggest that IFT protein function is conserved during PE formation in mouse and zebrafish and that, in zebrafish, IFT88 contributes to this process independently of its ciliary function.

To test whether IFT complex B affected other cardiac tissues, we focused in the myocardium. Cell quantification showed increased myocardial cell number in *ift88^{-/-}* compared to their controls at 50 hpf (**Fig. 2 A, A'**) and 55 hpf (**Supp. 4 A**). Interestingly, the increment was mostly affecting the atrium. Similar data were obtained with the *elipsa* mutants at 55hpf (**Fig. 2 B**). These results led us to conclude that the absence of IFT complex B proteins also affects the myocardial cells.

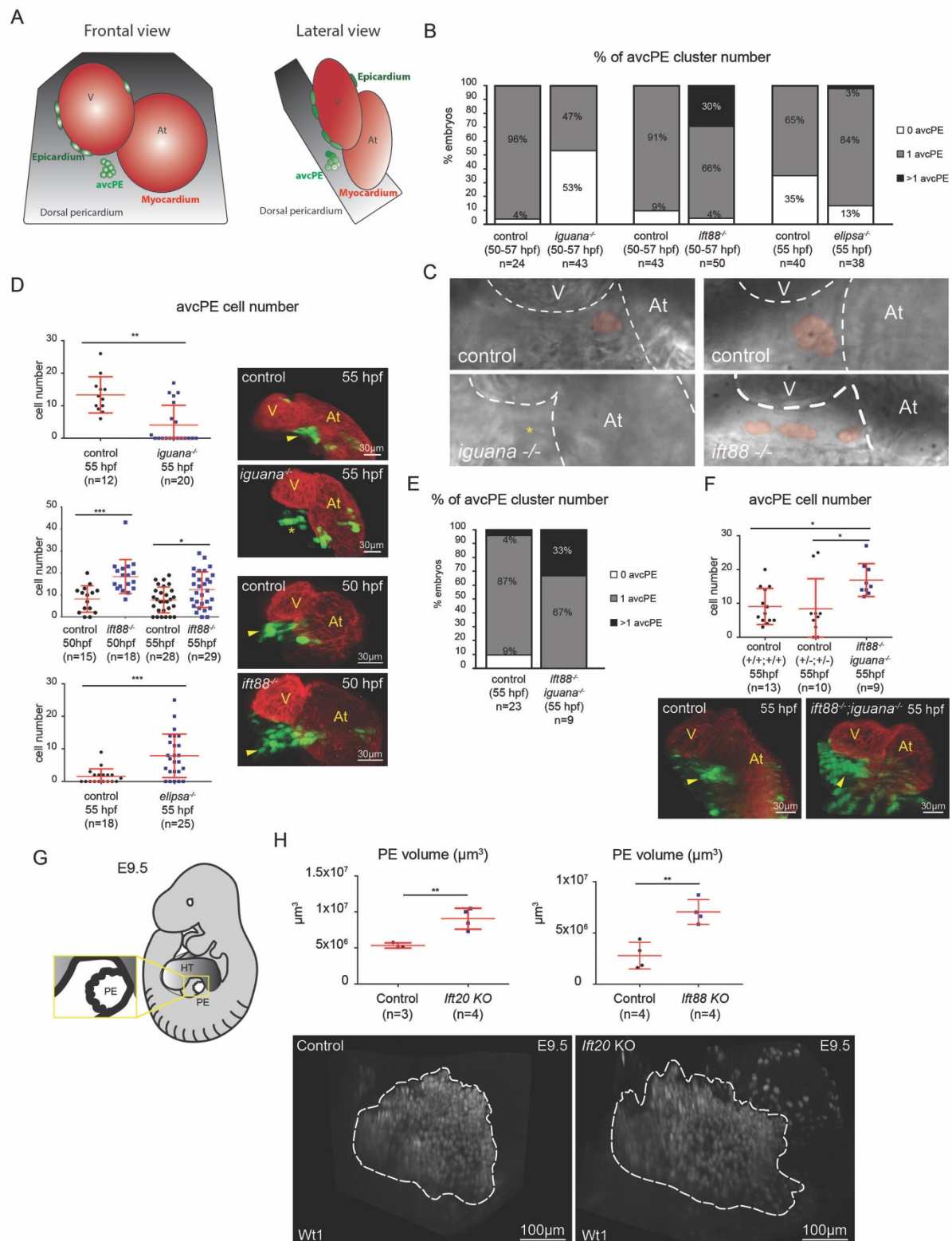


Figure 1. IFT complex B proteins regulate proepicardial development in zebrafish and mice.

(A) Schematic representation of the zebrafish heart at 55 hpf in frontal and lateral views. The dorsal pericardium is shown in grey, the myocardium in red, the avcPE in light green and the

151 epicardial cells in dark green. *V*, ventricle; *At*, atrium. **(B)** Percentage of *avcPE* cluster number
152 in *iguana* ($n=43$), *ift88* ($n=50$) and *elipsa/ift54* ($n=38$) mutants and their controls ($n=24$; $n=43$;
153 $n=40$ respectively), between 50 and 57 hpf. **(C)** High-speed *avcPE* imaging (digital red mask
154 to improve visualization) of *iguana* and *ift88* mutants and their control. **(D)** Graphs show *avcPE*
155 cell number quantified on *iguana* ($n=20$), *ift88* ($n=18$ and 29) and *elipsa* ($n=25$) mutants in
156 *epi:GFP* background and their controls ($n=12$; $n=15$; $n=28$ $n=18$ respectively). (t-test *iguana*
157 p -value 0.001; *ift88* p -value 0.0002 and p -value 0.015 respectively; *elipsa* p -value 0.0005). 3D
158 projections of whole mount immunofluorescence of hearts using an anti-myosin heavy chain
159 antibody (red) and GFP (green) expression. Ventral views, anterior is to the top. Arrowheads
160 mark *avcPE* and asterisk shows lack of *avcPE*. **(E)** Percentage of *avcPE* cluster number on
161 *iguana*^{-/-}, *ift88*^{-/-}, *epi:GFP* ($n=9$) and controls ($n=23$) at 55 hpf. **(F)** Graph shows *avcPE* cell
162 number quantified in wild type ($n=13$) and double heterozygous controls ($n=10$) (*ift88*^{+/+};
163 *iguana*^{+/+}; *epi:GFP* and *ift88*^{+/+}; *iguana*^{+/+}; *epi:GFP*) and double *ift88*; *iguana* mutants ($n=9$)
164 (*ift88*^{-/-}; *iguana*^{-/-}; *epi:GFP*) (Kruskal-Wallis p -value 0.014) . 3D projections of whole mount
165 immunofluorescence of hearts using myosin heavy chain antibody (red) and GFP (green)
166 expression. Ventral views, anterior is to the top. Arrowheads mark *avcPE*. *V*, ventricle; *At*,
167 atrium. **(G)** Schematic representation of an E9.5 mouse embryo. Heart tube (HT) in dark grey
168 and PE in white. Section of the PE represented inside the yellow box. **(H)** Left side graph shows
169 quantification of PE volume (μm^3) in *Ift20* KO ($n=4$) and control mice ($n=3$) (control
170 $5.35 \times 10^6 \mu\text{m}^3 \pm 3.63 \times 10^5$; *Ift20* KO $9.06 \times 10^6 \mu\text{m}^3 \pm 1.46 \times 10^6$) (t-test p -value 0.008) and that of
171 *Ift88* KO ($n=4$) and control embryo ($n=4$) on the right (control $2.78 \times 10^6 \mu\text{m}^3 \pm 1.3 \times 10^6$; *Ift88*
172 KO $7.05 \times 10^6 \mu\text{m}^3 \pm 1.2 \times 10^6$) (t-test p -value 0.003). In the lower panel, 3D projections of
173 immunofluorescence whole-mount performed on control and *Ift20* KO embryos. PE marked
174 using anti-*Wt1* antibody. White dotted shapes enclose the PE area. In all graphs, red bars
175 indicate mean \pm standard deviation.

176

177 *BMP signaling is increased in ift88, elipsa/ift54 and Ift20 mutants during PE development.*

178 As it is known in zebrafish that overexpressing BMP increases PE size (50), we investigated
 179 whether *ift88* loss influences BMP signaling. We first assessed *bmp4* expression by *in situ*
 180 hybridization in *ift88* and *elipsa* mutants. We found that *ift88* mutant embryos display ectopic
 181 expression of *bmp4* in the dorsal pericardium (DP) at 48 hpf (**Supp. 4 B**). To validate that the
 182 upregulation is functional *in vivo*, we quantified cellular BMP activity by using p-smad 1/5 as
 183 a readout and confirmed that the absence of Ift88 leads to increased BMP signaling activity
 184 (**Fig. 2 D, D'**). Additionally, more myocardial cells were positive for p-smad 1/5 in *ift88*^{-/-} than
 185 in controls, especially in the venous pole (**Fig. 2 D, D'**) (**Supp. 4 C**). By 55 hpf, *bmp4*
 186 expression at the atrioventricular canal myocardium is reduced and the expression at the venous
 187 pole is almost undetectable in controls. By contrast, *ift88* mutants presented strong *bmp4*
 188 expression in both domains (**Supp. 4 B**). Myocardial p-smad 1/5 was also increased in *ift88*^{-/-}
 189 compared to controls, but not in the DP (**Supp. 4 C, D**). We reached similar conclusions when
 190 analyzing the *elipsa* mutants at 55 hpf (**Fig. 2 E**) (**Supp. 4 B-C**). To confirm that the regulation
 191 of BMP signaling by IFT is conserved in vertebrates, we next analyzed p-smad 1/5/9 in *Ifi20*
 192 and *Ifi88 KO* and control mice at E9.5 and found that only the *Ifi20* mutants displayed a higher
 193 percentage of p-smad-positive cells compared to controls (**Fig. 2 G, G'**). (**Supp. 3 D**). Together,
 194 these results suggest that Ift88 and Ift54 modulate BMP signaling activity in the myocardium
 195 and the pericardium of the zebrafish, and that IFT20 plays a similar role in the mouse PE.

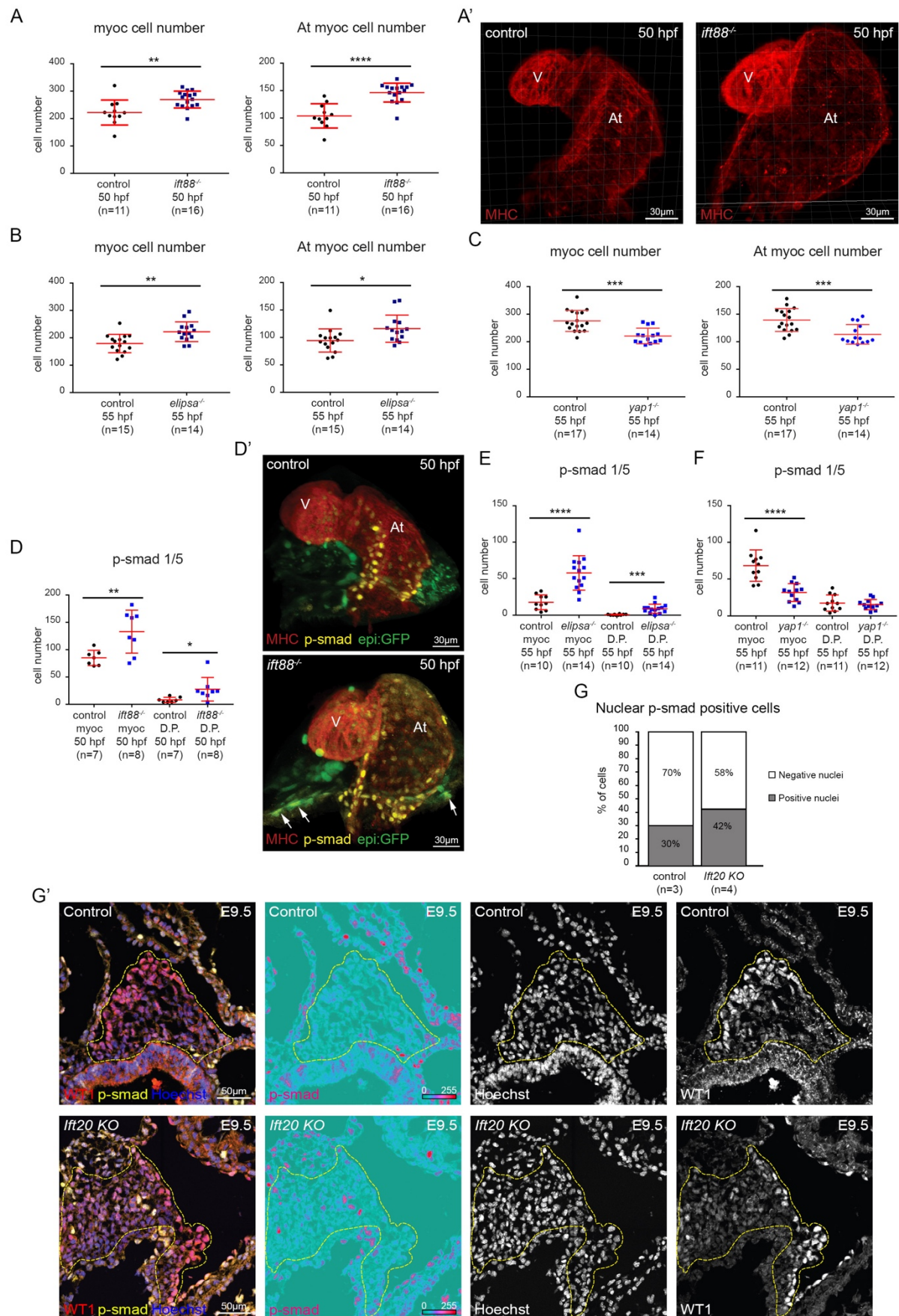


Figure 2. BMP signaling is increased in *ift88*, *elipsa/ift54* and *Ift20* mutants.

198 **(A)** Graphs show total myocardial and atrial-myocardial cell number quantified in *ift88* ($n=16$)
199 mutants and controls ($n=11$) at 50 hpf. (t-test total myocardium p-value 0.0034; atrial
200 myocardium p-value <0.0001). **(A')** 3D projections of whole mount immunofluorescence of
201 hearts using myosin heavy chain antibody (MHC) (red). Ventral views, anterior is to the top.
202 **(B)** Graphs show total myocardial and atrial-myocardial cell number quantified in *elipsa*
203 ($n=14$) mutants and controls ($n=15$) at 55 hpf. (t-test total myocardium p-value 0.0026; atrial
204 myocardium p-value 0.017). **(C)** Graphs show total myocardial and atrial-myocardial cell
205 number quantified in *yap1* ($n=14$) mutants and controls ($n=17$) at 55 hpf. (t-test total
206 myocardium p-value 0.0001; atrial myocardium p-value 0.0009). **(D)** Graph shows number of
207 p-smad1/5 positive cells in the myocardium and dorsal pericardium (DP) quantified in *ift88*
208 mutants ($n=8$) and controls ($n=7$) at 50 hpf. Myocardium (t-test p-value 0.009) and DP (t-test
209 p-value 0.036). **(D')** 3D projections of whole mount immunofluorescence of hearts using myosin
210 heavy chain antibody (MHC) (red), epi:GFP (green) and p-smad1/5 (yellow) antibody. Arrows
211 mark dorsal pericardial cells positive for epi:GFP and p-smad1/5. Ventral views, anterior is to
212 the top. **(E)** Graph shows number of p-smad1/5 positive cells in the myocardium and dorsal
213 pericardium (DP) quantified in *elipsa* mutants ($n=14$) and controls ($n=10$) at 55 hpf.
214 Myocardium (t-test p-value <0.0001) and DP (t-test p-value 0.0004). **(F)** Graph shows number
215 of p-smad1/5 positive cells in the myocardium and dorsal pericardium (DP) quantified in *yap1*
216 mutants ($n=12$) and controls ($n=11$) at 55 hpf. Myocardium (t-test p-value <0.0001) and DP
217 (t-test p-value 0.599). **(G)** Graph shows that the percentage of p-smad 1/5/9 positive PE cells
218 is higher in *Ift20* KO ($n=4$ embryos: 1862 nuclei analyzed) compared to control ($n=3$ embryos:
219 1414 nuclei analyzed) mice (Chi-square test of homogeneity =51.593, p-value $6.829e-13$ on 1
220 degree of freedom). **(G')** Control and *Ift20* KO immunofluorescence confocal cryosections
221 labelled with WT1 (red), p-smad 1/5/9 (yellow) and Hoechst (blue) at E9.5. Yellow dotted lines
222 enclose the PE area. Individual channels are displayed for p-smad 1/5/9 (signal is shown as

ice LUT to facilitate the visualization of signal intensity, where green is the minimum and red is the maximum), Hoechst (white) and *WT1* (white). In all graphs, red bars indicate mean \pm standard deviation. *V*, ventricle; *At*, atrium. *p-smad*, *p-smad1/5* in panel D' and *p-smad1/5/9* in panel G'.

Yap1-Tead activity is increased in *ift88*, *elipsa/ift54* and *Ift20* mutants during PE development.

YAP1/WWTR1, which are important regulators of tissue size (60), are essential for epicardium and coronary vasculature development (26). In addition, Yap1 participates in the regulation of Bmp signaling during secondary heart field development (21). This led us to assess if Yap1/Wwtr1-Tead is active during PE formation. We first analyzed Yap1/Wwtr1-Tead activity in PE cells using the *4xGTIIIC:d2GFP* reporter line (61). We found that the reporter was active in the PE cluster, myocardium, pericardium and epicardial cells at 55 hpf (**Supp. 5 A**). Time-lapse analysis allowed us to evaluate the dynamics of Yap1/Wwtr1-Tead activity during PE development between 51 and 60 hpf (**Movie 4**) (**Supp. 5 B**). GFP quantification in PE and pericardial cells showed higher Yap1/Wwtr1-Tead activity (GFP average intensity) in the PE cells than in the pericardial cells (75% of the embryos) (**Supp. 5 B**) (**Supp. Table 1**). Thus, Yap1/Wwtr1-Tead is active in PE cells during PE development.

We next tested whether the increased *avcPE* cell number was due to abnormal Yap1 activity, we performed immunofluorescence to quantify the number of nuclear Yap1-positive cells in *ift88* and *elipsa* mutants (**Fig. 3A, A'**) (**Supp. 6 A-B'**). At 55 hpf, *ift88*^{-/-} showed more nuclear Yap1-positive cardiomyocytes than controls (**Fig. 3 A**), especially in the atrium (**Supp. 6 A**). Similar data were obtained with the *elipsa* mutants (**Fig. 3 A**) (**Supp. 6 A**). To further validate the link between increased PE size and Yap1-Tead activity, we treated the *ift88* mutants with the drug Verteporfin, which binds to YAP and changes its conformation, blocking its interaction with TEAD (62). We first performed time-lapse imaging on Verteporfin treated

248 *4xGTIIIC:d2GFP* embryos at 55 hpf to assess Verteporfin specificity. We measured the
 249 Yap/Wwtr1-Tead activity (GFP average intensity) in the same PE and pericardial cells at
 250 several timepoints: before adding Verteporfin (t0), after 2 hours treatment with Verteporfin
 251 (5μM), and 45 min after washing out (**Supp. 5 C**). We found that Yap/Wwtr1-Tead activity is
 252 significantly decreased with Verteporfin, confirming the specificity of the drug on the embryo.
 253 We next treated *ift88*^{-/-} and control (*ift88*^{+/+} and ^{+/-}) embryos with Verteporfin (5μM) from 50
 254 hpf to 55 hpf (**Fig. 3 B**). Control embryos treated with Verteporfin showed smaller avcPE
 255 compared to untreated controls. Verteporfin-treated *ift88*^{-/-} embryos presented fewer avcPE cell
 256 numbers than non-treated *ift88*^{-/-} embryos. Interestingly, non-treated controls and treated *ift88*
 257 mutants did not show significant differences in avcPE cell number. Thus, the increase in avcPE
 258 cell number induced in the absence of Ift88 was rescued by Verteporfin treatment. These results
 259 suggest that Ift88 requires Yap1 activity to modulate the PE size restriction.
 260 Additionally, to explore a possible role of Yap1 in the regulation of BMP signaling by IFT, we
 261 treated *ift88*^{-/-} and control (*ift88*^{+/+} and ^{+/-}) embryos with Verteporfin (20μM) from 31 hpf to 55
 262 hpf (**Fig. 3 C**). We quantified cellular BMP activity by using p-smad 1/5 as a readout. Control
 263 embryos treated with Verteporfin showed decreased p-smad 1/5-positive myocardial cell
 264 number compared to untreated controls. Verteporfin-treated *ift88*^{-/-} embryos presented fewer p-
 265 smad 1/5-positive myocardial cells than non-treated *ift88*^{-/-} embryos. Remarkably, non-treated
 266 controls and treated *ift88* mutants did not show significant differences in p-smad 1/5-positive
 267 myocardial cells. Thus, the increase in BMP activity induced in the absence of Ift88 was rescued
 268 by Verteporfin treatment. Likewise, *in situ* hybridization performed in *elipsa*^{-/-} and control
 269 (*elipsa*^{+/+} and ^{+/-}) embryos treated with Verteporfin (20μM) from 31 hpf to 55 hpf displayed
 270 decreased *bmp4* expression (**Supp. 6 C**). Furthermore, treatment with the drug XAV939
 271 (10μM), a tankyrase inhibitor that suppressed YAP-TEAD activity (63) also lead to a reduction
 272 of *bmp4* expression (**Supp. 6 C**). These results suggest that Ift88 and Ift54 require Yap1 activity

to modulate BMP signaling activity in the myocardium of the zebrafish. To confirm the involvement of an increased Yap1 activity in the *ift88* mutant phenotype, we analyzed the avcPE in *angiomin like 2a* (*amotl2a*) mutants (**Fig. 3 D, E**). In zebrafish, Amotl2a physically interacts with Yap1 leading to its cytoplasmic retention in a way that *amotl2a* mutants show upregulated Yap1 activity (nuclear Yap1) (33,34). Accordingly, *amotl2a*^{-/-} presented multiple avcPE formation. In addition, *bmp4* expression was increased in *amotl2a*^{-/-} when compared to *amotl2a*^{+/+} embryos at 55 hpf. These data are consistent with the *ift88* mutant phenotype and suggest that Ift88 modulates Yap1 activity to restrict PE size. To further validate the link between increased Yap1 and BMP signaling activity, we treated the *amotl2a* mutants with the drug Verteporfin (20μM) from 31 hpf to 55 hpf (**Fig. 3 F, F'**). *amotl2a*^{-/-} embryos treated with Verteporfin showed decreased p-smad 1/5-positive myocardial cell number and avcPE cells compared to untreated *amotl2a*^{-/-} embryos. Likewise, *bmp4* expression at the atrioventricular canal myocardium and at the venous pole were reduced in *amotl2a*^{-/-} embryos treated with XAV939 (10μM) from 31 hpf to 55 hpf, when compared to untreated *amotl2a*^{-/-} embryos (**Fig. 3 G**). Thus, Verteporfin and XAV939 treatments rescued the increase in BMP signaling induced in the absence of Amotl2a suggesting it acts through Yap1 activity. To further confirm the link between Yap1 activity and PE formation, we next analyzed the *yap1* mutants (33). At 55 hpf, *yap1*^{-/-} showed decreased myocardial cell number compared to their controls (**Fig. 2 C**). Besides, fewer myocardial cells were positive for p-smad 1/5 in *yap1* mutants (**Fig. 2 F**). Surprisingly, avcPE cell number was similar between *yap1*^{-/-} and their controls (**Supp. 2 B, B'**). Altogether, these results suggest that Ift88 and Ift54 modulate BMP signaling activity by tuning Yap1-Tead activity in the myocardium of the zebrafish. To assess if the upregulation of Yap1 activity observed in IFT zebrafish mutants was conserved in vertebrates, we analyzed YAP1 localization in the PE of *Ifi20 KO* and control mice (**Fig. 3 H-H''**). We quantified the proportion of nuclear YAP1-positive cells (i.e. cells with higher signal intensity inside the nucleus than in

the cytoplasm) (**Fig. 3 H''**). The percentage of nuclear YAP1-positive PE cells was higher in *Ift20 KO* than in control mice (**Fig. 3 H**). In mouse cardiomyocytes, YAP1 and AMOTL1 translocate to the nucleus together to modulate cell response (23). To assess AMOTL1 localization in PE cells, we performed AMOTL1 immunofluorescence. Consistent with the results obtained with an anti-YAP1 antibody, the percentage of nuclear AMOTL1-positive cells (i.e. cells with higher signal intensity inside the nucleus than in the cytoplasm) was increased in the *Ift20 KO* when compared to control mice (**Supp. 6 D**). We also found that the mutants showed an increase in the percentage of YAP1–AMOTL1 double positive cells (**Fig. 3 H**). Together, these data show that the increased PE size in *Ift20 KO* mice is associated with increased YAP1 activity.

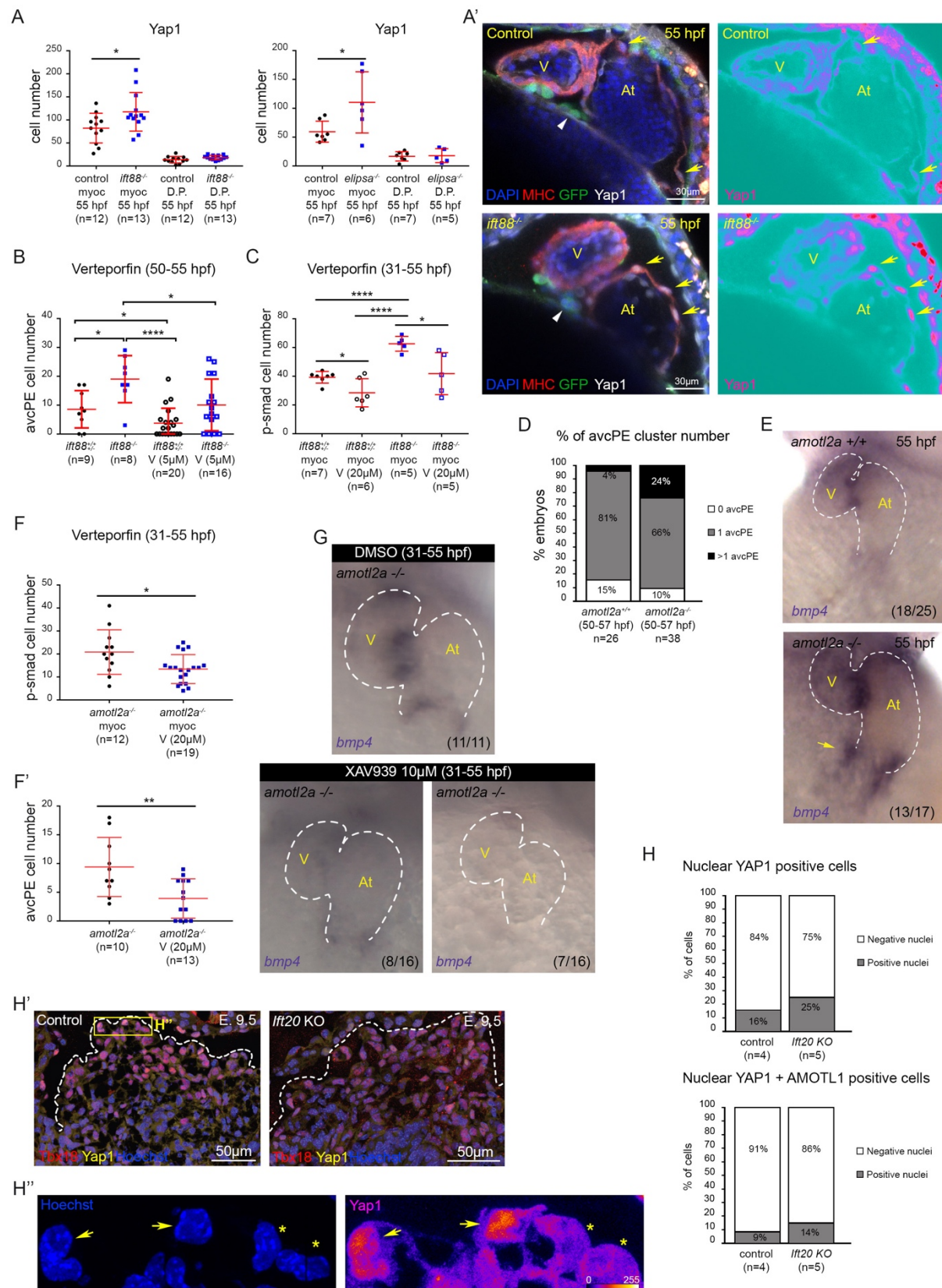


Figure 3. Yap1-Tead activity is increased in *ift88*, *elipsa/ift54* and *Ifi20* mutants during proepicardium development.

312 **(A)** Graphs show number of Yap1-positive cells in the myocardium and dorsal pericardium
313 (DP) quantified in *ift88* (n=13), *elipsa* (n=6) and their controls (n=12 and n=7 respectively).
314 *ift88* mutants show increased Yap1-positive myocardial cell numbers (t-test p value 0.03) and
315 a tendency towards higher Yap1 positive DP cell numbers (t-test p value 0.07). *elipsa* mutants
316 show higher Yap1-positive myocardial cell numbers (t-test p value 0.036). **(A')** Control and
317 *ift88*^{-/-}, *epi:GFP* immunofluorescence confocal sections labelled with anti-myosin heavy chain
318 antibody (MHC) (red), GFP (green), -Yap1 (white) and DAPI (blue) at 55 hpf. Ventral view,
319 anterior is to the top. Individual channel is displayed for Yap1 (signal is shown as ice LUT to
320 facilitate the visualization of signal intensity, where green is the minimum and red is the
321 maximum). Yellow arrows mark nuclear Yap1-positive atrial myocardial cells. White
322 arrowheads mark the avcPE. **(B)** Graph shows avcPE cell number quantified in control (n=9),
323 *ift88*^{-/-}, *epi:GFP* (n=8) and Verteporfin (5μM)-treated *ift88*^{-/-}, *epi:GFP* (n=16) and control
324 (n=20) embryos (55hpf). Control embryos treated with Verteporfin showed smaller avcPE
325 compared to untreated controls (t-test p-value 0.04). Verteporfin-treated *ift88*^{-/-}, *epi:GFP*
326 embryos presented lower avcPE cell numbers than non-treated *ift88*^{-/-}, *epi:GFP* embryos (t-test
327 p-value 0.027). *ift88*^{-/-}, *epi:GFP* embryos showed bigger avcPE compared to untreated (t-test
328 p-value 0.01) and treated controls (t-test p-value 0.0001). **(C)** Graph shows number of p-smad
329 1/5-positive cells in the myocardium quantified in control (n=7), *ift88*^{-/-}, *epi:GFP* (n=5) and
330 Verteporfin (20μM)-treated *ift88*^{-/-}, *epi:GFP* (n=5) and control (n=6) embryos from 31 hpf to
331 55 hpf. Control embryos treated with Verteporfin showed decreased p-smad 1/5-positive cell
332 numbers compared to untreated controls (t-test p-value 0.0219). Verteporfin-treated *ift88*^{-/-},
333 *epi:GFP* embryos presented less p-smad 1/5-positive cells than non-treated *ift88*^{-/-}, *epi:GFP*
334 embryos (t-test p-value 0.0173). *ift88*^{-/-}, *epi:GFP* embryos showed more p-smad 1/5-positive
335 cells compared to untreated (t-test p-value <0.0001) and treated controls (t-test p-value
336 <0.0001). **(D)** Percentage of avcPE cluster number in *amotl2a*^{+/+} (n=26) and *amotl2a*^{-/-} (n=38)

embryos between 50 and 57 hpf. **(E)** Whole mount *bmp4* in situ hybridization in *amotl2a*^{+/+} (n=18/25) and *amotl2a*^{-/-} (n=13/17) embryos (55hpf). Yellow arrow shows *bmp4* overexpression. Ventral views, anterior is to the top. **(F)** Graph shows number of p-smad 1/5-positive cells in the myocardium quantified in Verteporfin (20μM)-treated *amotl2a*^{-/-} (n=19) embryos from 31 to 55 hpf and untreated *amotl2a*^{-/-} (n=12) embryos. Treated embryos showed decreased p-smad 1/5-positive cell numbers compared to untreated ones (t-test p-value 0.0148). **(F')** Graph shows avcPE cell number quantified in Verteporfin (20μM)-treated *amotl2a*^{-/-} (n=13) embryos from 31 to 55 hpf and untreated *amotl2a*^{-/-} (n=10) embryos. Treated embryos showed decreased avcPE cell numbers compared to untreated ones (t-test p-value 0.0059). **(G)** Whole mount *bmp4* in situ hybridization in XAV939 (10μM)-treated *amotl2a*^{-/-} (n=16) from 31 to 55 hpf and untreated embryos (n=11). Treated embryos showed either decreased (n=8/16) or absent (n=7/16) *bmp4* expression at the atrioventricular canal myocardium and the venous pole. Ventral views, anterior is to the top. **(H)** Graphs show percentages of YAP1-positive PE cells and double YAP1-AMOTL1-positive PE cells in *Ifi20* KO (n=5 embryos: 1196 nuclei analyzed) and control (n=4 embryos: 929 nuclei analyzed) mice at E9.5. The percentage of nuclear YAP1-positive PE cells (Chi-square test of homogeneity =25.354, p-value 4.77E-07 on 1 degree of freedom) and nuclear YAP1-AMOTL1-positive cells (Chi-square test of homogeneity =12.025, p-value 5.25E-04 on 1 degree of freedom) were higher in *Ifi20* KO than in control mice. **(H')** Control and *Ifi20* KO immunofluorescence confocal cryosections labelled with TBX18 (red), YAP1 (yellow) and Hoechst (blue) at E9.5. White dotted lines enclose the PE area. **(H'')** Zoomed region shows the difference between nuclear YAP1-positive cells (yellow arrows) and YAP1-negative cells (yellow asterisks). Hoechst signal (blue) highlights cell nuclei. YAP1 signal is shown as fire LUT to facilitate the visualization of signal intensity, where blue is the minimum and yellow is the maximum. In all graphs, red bars indicate mean ± standard deviation.

IFTs interact with YAP1 and regulate its activity.

Taking advantage of cultured cells, we next explored the mechanism by which IFT proteins could regulate YAP1 activity. Immunofluorescence performed in HeLa cells transfected with IFT88-GFP, showed co-localization between IFT88 and YAP1 in the cytoplasm (**Supp. 7 A-C**). To confirm a potential physical interaction between IFT proteins with YAP1, we first performed Co-IP experiments using IFT88-GFP and YAP1-Myc in HeLa cells but never obtained any clear interaction. Considering that YAP1 often necessitates the scaffold protein Angiomotin-like 1 (Amotl1) (23), we next performed Co-IP experiment using HA-Amotl1, IFT88-GFP, and YAP1-Myc in HeLa cells. The experiments revealed a clear interaction between YAP1, Amotl1, and IFT88 (**Fig. 4 A**). Similarly, physical interaction between endogenous YAP1, Flag-Amotl1, and IFT20-GFP was observed in transfected HEK293 cells (**Fig. 4 A**). Together, these results reveal that IFT proteins, YAP1, and Amotl1 could function as part of a complex involved in the functional modulation of YAP1 activity *in vivo*.

To functionally assess the impact of endogenous IFT88 depletion on YAP1 activity, we next used a DLD-1 IFT88-auxin-inducible degron (AID) cell line, in which a rapid degradation of IFT88 protein can be induced by auxin treatment (**Fig. 4 B**). Of note, DLD-1 cells don't grow cilia allowing us to explore the cytoplasmic, cilia independent function of IFT88 (64).

We observed that 2 hours of auxin treatment led to IFT88 and YAP1 degradation. The rapid co-degradation further suggested that both proteins physically interact (**Fig. 4 C**). We confirmed this finding by performing shorter auxin treatments to study the progressive degradation of IFT88 and YAP1 (**Fig. 4 C'**). Importantly, as previously observed *in vivo*, longer depletion of endogenous IFT88 after 6 hours of auxin treatment led to an increase in nuclear YAP1 measured by immunofluorescence (**Fig. 4 D**) (**Supp. 8 A**). Consistently, the nuclear/cytoplasmic YAP1 ratio was also increased (**Supp. 8 A**). Additionally, we confirmed these results using HeLa and

MDCK cell lines where IFT88 function was inactivated by IFT88-siRNA. The IFT88-siRNA efficiency was validated by immunofluorescence and western blot (Supp. 9 A-C). After 48 hours of IFT88-siRNA treatment, nuclear YAP1 signal was measured by immunofluorescence (Fig. 4 E-F'). The inactivation of IFT88 was accompanied with increased nuclear YAP1 (Fig. 4 E, F). Altogether, these data indicate that IFT88 can interact with YAP1 in the cytoplasm and is involved in modulating the activation of the Hippo pathway effector YAP1.

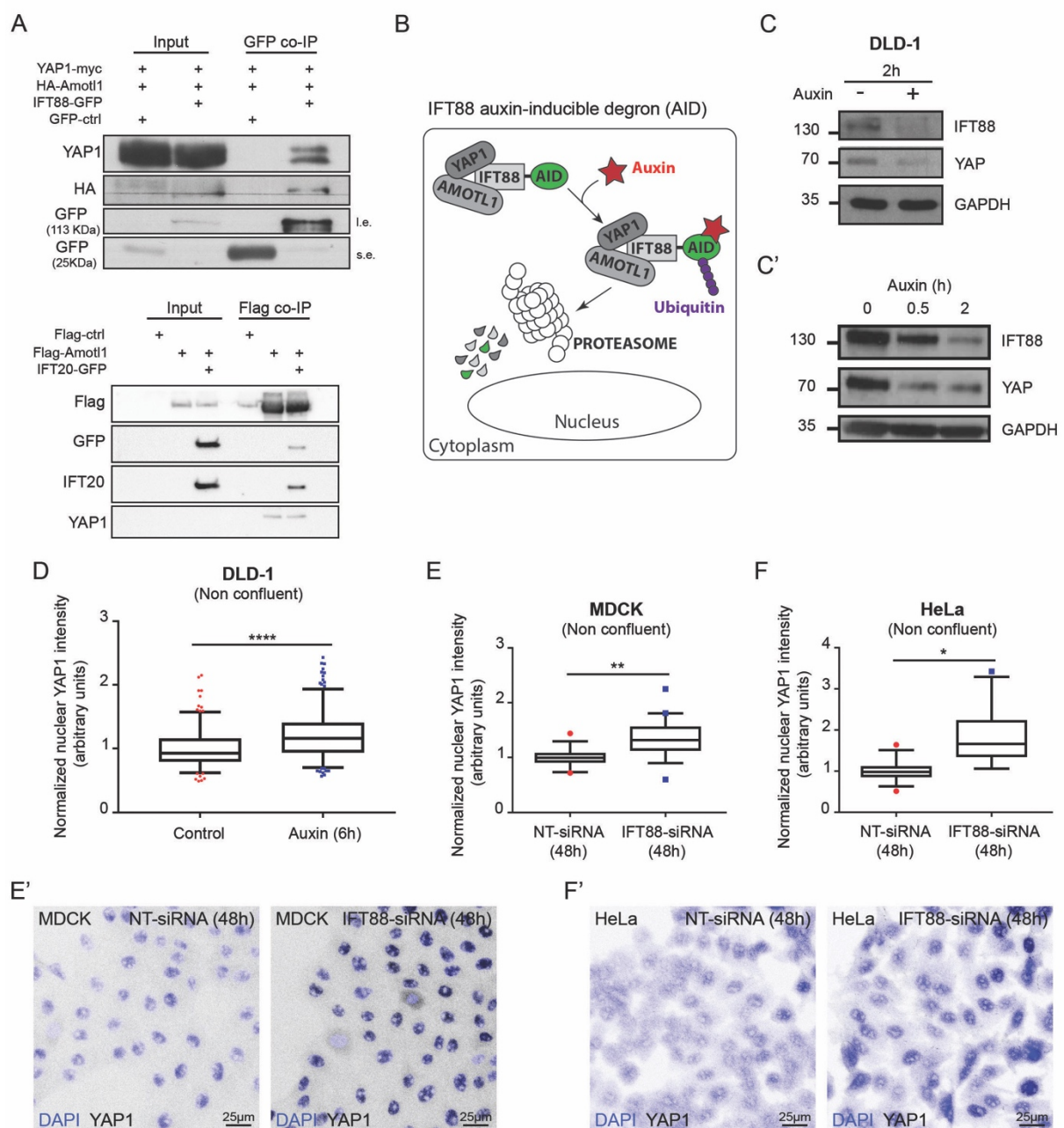


Figure 4. IFT88 and IFT20 are physically associated to YAP1 and IFT88 modulates YAP1 activity.

(A) Co-IP experiment using HeLa cells transfected with IFT88-GFP, HA-Amotl1 and YAP1-Myc. (l.e. = long exposure. s.e. = short exposure). Co-IP experiment using HEK293 cells transfected with Flag-Amotl1 and IFT20-GFP. Endogenous levels of Yap1 are monitored. **(B)** Schematic representation of the IFT88 auxin-inducible degron (AID) system **(C)** Western blot analysis of IFT88 AID DLD-1 cells after 2 hours auxin treatment. **(C')** Western blot analysis of IFT88 and YAP1 degradation after auxin treatment (0 h, 0.5h and 2 h). **(D)** Graph shows the increase in normalized YAP1 nuclear signal in cells treated with auxin (6h) (Mann-Whitney p-value <0.0001). (controls: 2 replicates, n=204 cells; Auxin 2h: 2 replicates, n=261 cells). **(E)** Graph shows the increase in YAP/WWTR1 (TAZ) nuclear signal in IFT88-siRNA (48h) treated MDCK cells (n=5 replicates, average cell number analyzed for each condition = 382, t-test p-value 0.004). Box and whiskers (5-95 percentile). Outliers are represented as red dots (NT-siRNA) or blue squares (IFT88-siRNA). **(E')** Immunofluorescence confocal images (z-projection) of MDCK cells treated with NT – or IFT88-siRNA (48h). DAPI (blue) and YAP/WWTR1 (TAZ) (white inverted LUT). **(F)** Graph shows the increase in YAP/WWTR1 (TAZ) nuclear signal in IFT88-siRNA (48h) treated HeLa cells (n=5 replicates, average cell number analyzed for each condition = 252, t-test p-value 0.02). Box and whiskers (5-95 percentile). Outliers are represented as red dots (NT-siRNA) or blue squares (IFT88-siRNA). **(F')** Immunofluorescence confocal images (z-projection) of HeLa cells treated with NT – or IFT88-siRNA (48h). DAPI (blue) and YAP/WWTR1 (TAZ) (white inverted LUT).

To confirm that increased nuclear YAP1 is specific of IFT protein function, we performed IFT88 and IFT20 overexpression assays. While the transfection of pEGFP C1 did not alter the nuclear signal between GFP-positive and GFP-negative cells (endogenous control) (**Supp. 6 D**)

(Supp. 7 B-D), IFT88-GFP and IFT20-GFP overexpression caused a decrease in nuclear signal (Supp. 7 C, D). Together, these data confirm that IFT proteins modulate YAP1 activation.

Discussion

Primary cilia function has long been implicated in the control of the developmental program, but whether cilia-related proteins could affect cell signaling independently of their ciliary function remains unclear. Here, we have shown that IFT complex B members, IFT88 and IFT20 modulate the Hippo pathway effector YAP1 in different cell types. We also demonstrated that IFT88 and IFT20 modulates PE size in mouse and that *Ift88* and *Ift54* do the same in zebrafish PE and myocardium. Mechanistically, work *in cellulo* suggest that IFT88 physically interacts with YAP1 to modulate its activity. Together, this work establishes a previously unknown role for IFT complex B proteins in regulating cell signaling and tissue growth during cardiogenesis and shed a novel light on cilia related protein function during cardiogenesis.

IFT proteins have long been associated with ciliary functions in developmental processes. For example, *ift88* mutants display a number of phenotypes reminiscent of ciliary defects such as abnormal patterning of the neural tube, defects in the Hedgehog pathway and left-right patterning (58). *Ift88* has also been associated with planar cell polarity (65) and cell division (15,16). Our observations that the *ift88* mutants show increased number of nuclear Yap1-positive cells in the myocardium and that the *Ift20* KO mice display increased nuclear Yap1/Amot1 – positive cells in the PE, provide evidences for a novel role of IFT complex B proteins in cardiogenesis. Mechanistically, IFT proteins are best known for their function in ciliary transport (66). Here, we describe an unexpected interaction between the ciliary machinery proteins and a potent mechanosensing pathway, the Hippo pathway. The hippo

445 effector YAP1 is known to have essential roles in cancer (67), regeneration (24,25,68), and
 446 organ size control (69–71). Several mechanisms have been shown to regulate the shuttling of
 447 YAP1 into the nucleus, including phosphorylation by Hippo kinases. Recent studies show that
 448 YAP1 is mechanosensitive and that force applied to the nucleus can directly drive YAP1
 449 nuclear translocation (27,72). Additionally, Angiomotin (AMOT) have been shown to interact
 450 physically with YAP1 and acts as a buffering factor sequestering YAP1 in the cytoplasm (31).
 451 Nevertheless, AMOTL1 has also been shown to co-localize with YAP1 in the nucleus (23,73)
 452 demonstrating YAP1 subcellular localization is highly regulated by Motin family proteins. Our
 453 results indicate that IFT complex B proteins are also involved in regulating YAP1 localization.
 454 We demonstrate that IFT88 interacts biochemically with YAP1 and both co-localize in the
 455 cytoplasm. We did not study TAZ, the other Hippo effector which is known to act with YAP1
 456 (74) and we cannot draw general conclusions on the role of IFT88 on all the known Hippo
 457 effectors. Nevertheless, our work suggests alternative ways to interpret Ift88 mutant phenotypes,
 458 which are often interpreted based on polarity or cilia function issues, and, more generally,
 459 phenotypes of other mutants with abnormal IFT complex B proteins. Our working model is that
 460 Ift88 participates in sequestering YAP1 away from the nucleus using its cargo transport activity.
 461 Other cilia related proteins such kinesin2 and IFT complex A proteins have been shown to
 462 promote nuclear localization of β -catenin during Wnt signaling in drosophila (75), further
 463 suggesting that proteins identified for their ciliary transport functions are not always limited to
 464 that function. Interestingly, IFT-A complexes control retrograde protein transport, from the tip
 465 to the base of the cilium (76–78), while the IFT-B complexes do the opposite, as observed for
 466 YAP1 transport towards the nucleus. Future work will reveal the mechanism by which Ift88
 467 limits nuclear translocation of YAP1 in this process and address whether IFT complex A
 468 proteins play a role.

Importantly, while our study points towards a non-canonical function for IFT complex B proteins, our results do not exclude a role for primary cilia in PE formation. We found that *iguana/dzip* mutants display a avcPE phenotype suggesting that primary cilia function is required for PE morphogenesis. The HH pathway is often associated with ciliary function. To date, a number of studies suggest the proepicardium and epicardium formation are not regulated by Hedgehog signaling (79,80). Indeed, dissection of zebrafish *shha* function in the PE and epicardium using a *tcf21:CreER*, a well-established PE and epicardial tissue driver (81), does not affect PE formation (80). Besides, expression of *Shh*, *Dhh*, *Ihh*, and *Ptch1* was neither detected in the mouse PE nor in the epicardium at subsequent stages (79). Thus, primary cilia certainly operate independently of the HH pathway in the process. Our work further highlights the important role of the BMP pathway in PE formation. BMP is essential for PE formation and morphogenesis (50,82). There is numerous evidence to suggest that primary cilia modulate BMP pathway and, more generally, TGF beta signaling pathways (83,84). In endothelial cells, primary cilia modulate angiogenesis by altering BMP signaling in endothelial cells (85). We speculate the situation is different in PE cells, where BMP is activated downstream of YAP1, and where IFT88 helps to limit YAP1 and BMP signaling. Similarly, secondary heart field development also depends on the modulation of Hippo signaling by BMPs (21).

In summary, our study is the first report implicating IFT complex B proteins during PE development by modulating YAP1 activity independently of any cilia function. A deeper understanding of the molecular mechanisms regulating PE development is of great importance, underlined by its role in myocardial maturation and coronary vessel formation during development, as well as the regenerative capacity of the heart (86). Considering that IFT proteins are often associated with ciliopathies, linking IFT with YAP1 activity might have important implications for understanding the etiology of ciliopathies during cardiogenesis and for the interpretation of ciliary defects in IFT mutants.

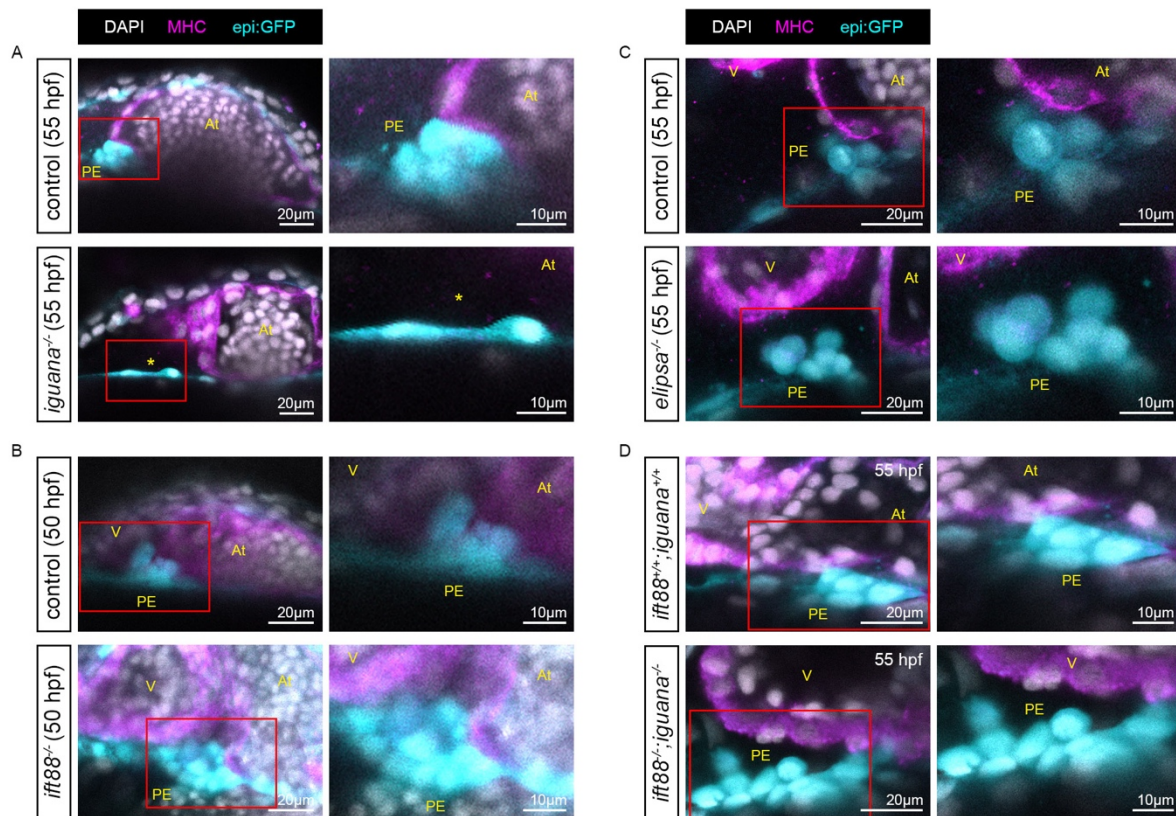
494

495 *Acknowledgements*

496 We thank P. Lamperti, E. Steed, A Bhat, D. Riveline, S. Harlepp, J. Godin, A. Benmerah and
 497 the Vermot lab for discussion and thoughtful comments on the manuscript, in particular R.
 498 Chow for her help with editing. We thank G. Pazour, M. Faucourt and N. Spassky for advice,
 499 the gift of plasmids and for providing the *Ifi20* and *Ifi88* mutant mouse lines and C. Cimper, L.
 500 Bombardelli and C. Shea for technical assistance. We are grateful to the IGBMC fish facility,
 501 the IGBMC imaging center and the imaging platforms of the SFR Necker. This project has
 502 received funding from the European Union’s Horizon 2020 research and innovation programme
 503 under the Marie Skłodowska-Curie grant agreement No 708312 (MP). This work was supported
 504 by FRM (DEQ20140329553), the European seventh framework program (ERC 682938 -
 505 EVALVE), ANR (ANR-15-CE13-0015 – liveheart) and by the grant ANR-10-LABX-0030-
 506 INRT, a French State fund managed by the Agence Nationale de la Recherche under the frame
 507 program Investissements d’Avenir labeled ANR-10-IDEX-0002–02. BD team was supported
 508 by ANR-12-CHEX-005 and CNRS. SM team was supported by core funding from the Institut
 509 *Imagine*, the Institut Pasteur, the INSERM, the Université Paris Descartes, and a grant from the
 510 AFM-Téléthon [Trampoline 18727]. TL was funded by the ED515 (1691/2014).

511

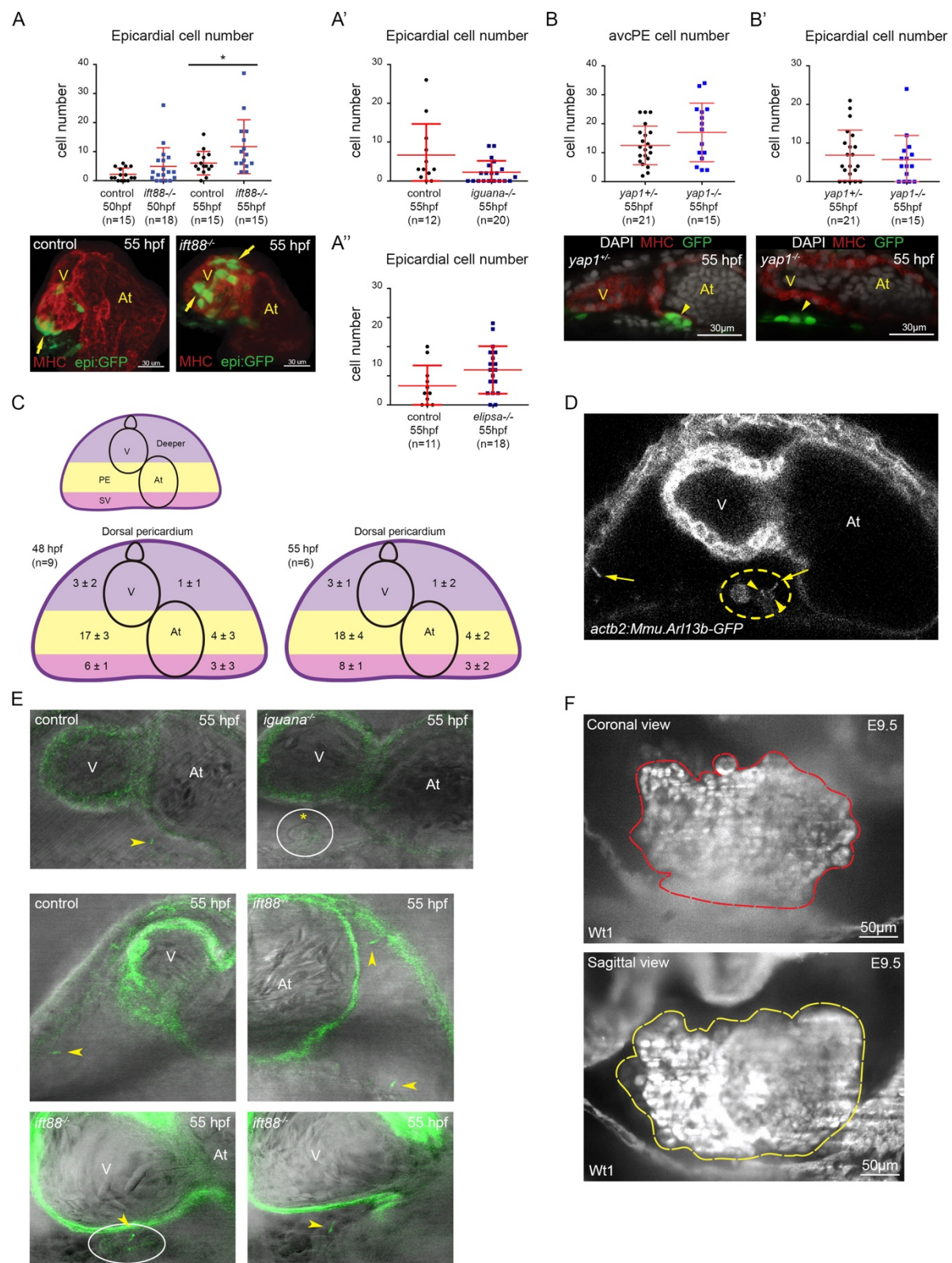
512



Supplementary Figure 1. IFT complex B mutants show increased proepicardial size in zebrafish.

(A) Confocal sections of whole mount immunofluorescence of *iguana*^{-/-}, epi:GFP and control using anti-myosin heavy chain antibody (MHC) (magenta), anti-GFP (cyan) and DAPI (white) antibodies at 55 hpf. Asterisk shows lack of avcPE as there is only one rounded PE cell. **(B)** Confocal sections of whole mount immunofluorescence of *ift88*^{-/-}, epi:GFP and control using anti-myosin heavy chain antibody (MHC) (magenta), anti-GFP antibody (cyan) and DAPI (white) at 50 hpf. **(C)** Confocal sections of whole mount immunofluorescence of *elipsa*^{-/-}, epi:GFP and control using anti-myosin heavy chain antibody (MHC) (magenta), anti-GFP (cyan) and DAPI (white) antibodies at 55 hpf. **(D)** Confocal sections of whole mount immunofluorescence of *ift88*^{-/-}, *iguana*^{-/-}, epi:GFP and *ift88*^{+/+}, *iguana*^{+/+}, epi:GFP using anti-myosin heavy chain antibody (MHC) (magenta), anti-GFP (cyan) and DAPI (white) antibodies

526 *at 55 hpf. All images are ventral views, anterior is to the top. V, ventricle; At, atrium; PE,*
527 *avcPE. Zoomed regions contained inside the red boxes are showed on the right side.*
528
529
530

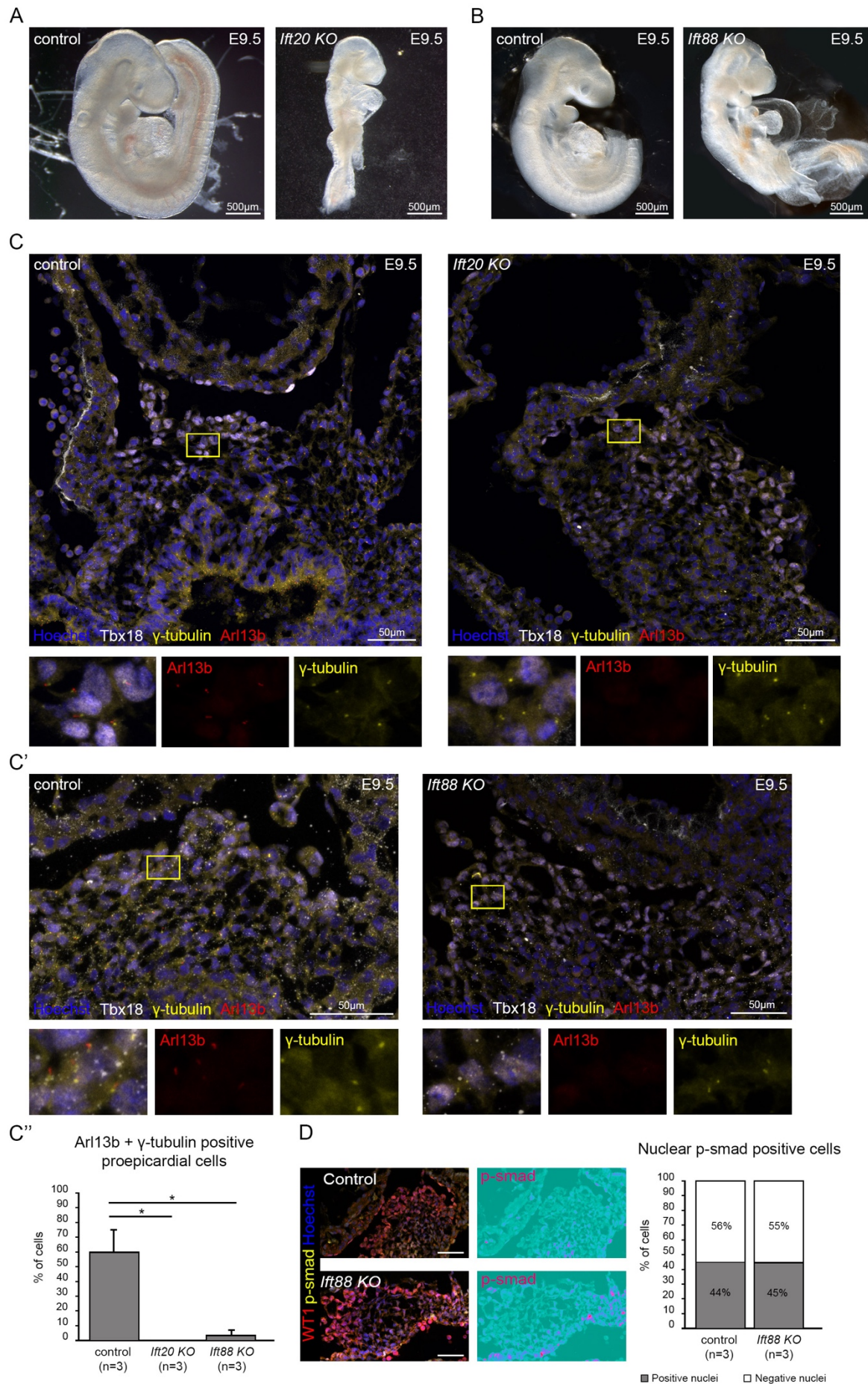


Supplementary Figure 2. Cilia protruding into the pericardial cavity are distributed heterogeneously in zebrafish during proepicardial development.

534 **(A-A'')** Graphs show epicardial cell numbers quantified in *ift88*, *iguana* and *elipsa* mutants in
535 *epi:GFP* background. **(A)** At 55 hpf, *ift88* mutants ($n=15$) showed increased epicardial cell
536 numbers (t -test p value 0.04). 3D projections of whole mount immunofluorescence of hearts
537 using anti-myosin heavy chain antibody (red) and GFP (green) expression. Ventral view,
538 anterior is to the top. Arrows mark some epicardial cells; **(A')** *iguana* mutants ($n=20$) showed
539 a tendency towards decreased epicardial cell numbers (t -test p value 0.055), while **(A'')** *elipsa*
540 mutants ($n=18$) showed a tendency towards increased epicardial cell number (t -test p value
541 0.08). **(B)** Graph shows *avcPE* cell numbers quantified in *yap1*^{-/-} ($n=15$) and control ($n=21$)
542 embryos in *tcf21:nsf-GFP* background at 55 hpf. (t -test p -value 0.12) Control and *yap1*^{-/-}
543 immunofluorescence confocal sections labelled with anti-myosin heavy chain antibody (MHC)
544 (red), GFP (green), DAPI (white). Ventral view, anterior is to the top. Yellow arrowheads point
545 at the *avcPE*. **(B')** Graph shows epicardial cell numbers quantified in *yap1*^{-/-} ($n=15$) and
546 control ($n=21$) embryos in *tcf21:nsf-GFP* background at 55 hpf. (Mann Whitney p -value 0.63)
547 **(C)** For cilia quantification, we divided the dorsal pericardial wall in to three different regions:
548 *SV* region, including the sinus venosus (pink); *PE* region, where the *avcPE* forms (yellow) and
549 *Deeper* region (purple). These three regions were subdivided in to right and left halves,
550 containing the ventricle or the atrium respectively. At 48 hpf ($n=9$ larvae), prior to *PE*
551 formation, cilia protruding from the dorsal pericardium showed a heterogeneous distribution.
552 Interestingly, the right half of the *SV* (6 ± 1) and the *PE* (17 ± 3) regions, where both *PE* clusters
553 will form, presented higher cilia number than the rest of the regions. At 55 hpf, when the *avcPE*
554 is formed, the cilia distribution was similar to that observed at 48 hpf ($n= 6$ larvae). **(D)**
555 Confocal section of *actb2:Mmu.Arl13b-GFP* embryo (55 hpf). Yellow dotted circle encloses the
556 *avcPE*. Yellow arrows point to cilia protruding from the ventral and dorsal pericardium. Yellow
557 arrowheads point at immotile and bent cilia protruding from a few *avcPE* cells. **(E)** Confocal
558 section of *iguana*; *actb2:Mmu.Arl13b-GFP* and control embryos (55 hpf). Yellow arrowhead

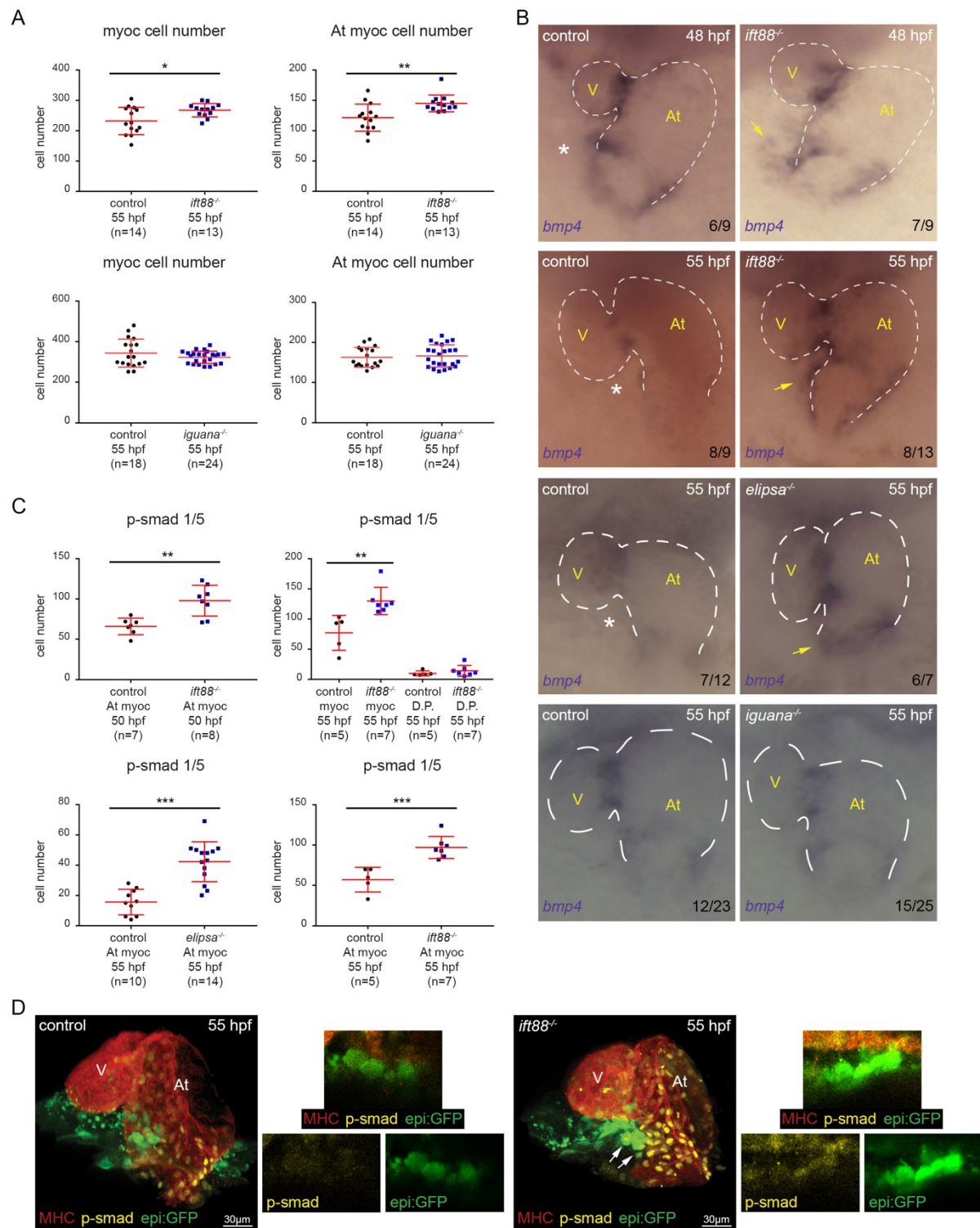
559 *points at cilium protruding from the avcPE. Yellow asterisk shows lack of cilia in the avcPE*
560 *(enclosed in the white circle). Confocal section of ift88; actb2:Mmu.Arl13b-GFP and control*
561 *embryos (55 hpf). In control embryo, yellow arrowhead points at cilium protruding from the*
562 *ventral pericardium. In ift88 mutant embryo, yellow arrowheads point at cilia protruding from*
563 *ventral and dorsal pericardium and the avcPE (enclosed in the white circle). (F) Coronal and*
564 *sagittal sections acquired by light sheet microscopy to illustrate the methods used to measure*
565 *PE volume (labeled with anti-Wt1 antibody). Red and yellow dotted shapes enclose the PE area.*
566 *In all images ventral views, anterior is to the top. V, ventricle; At, atrium. In all graphs, red*
567 *bars indicate mean \pm standard deviation.*

568



Supplementary Figure 3. *Ift20* KO mice proepicardial cells lack cilia.

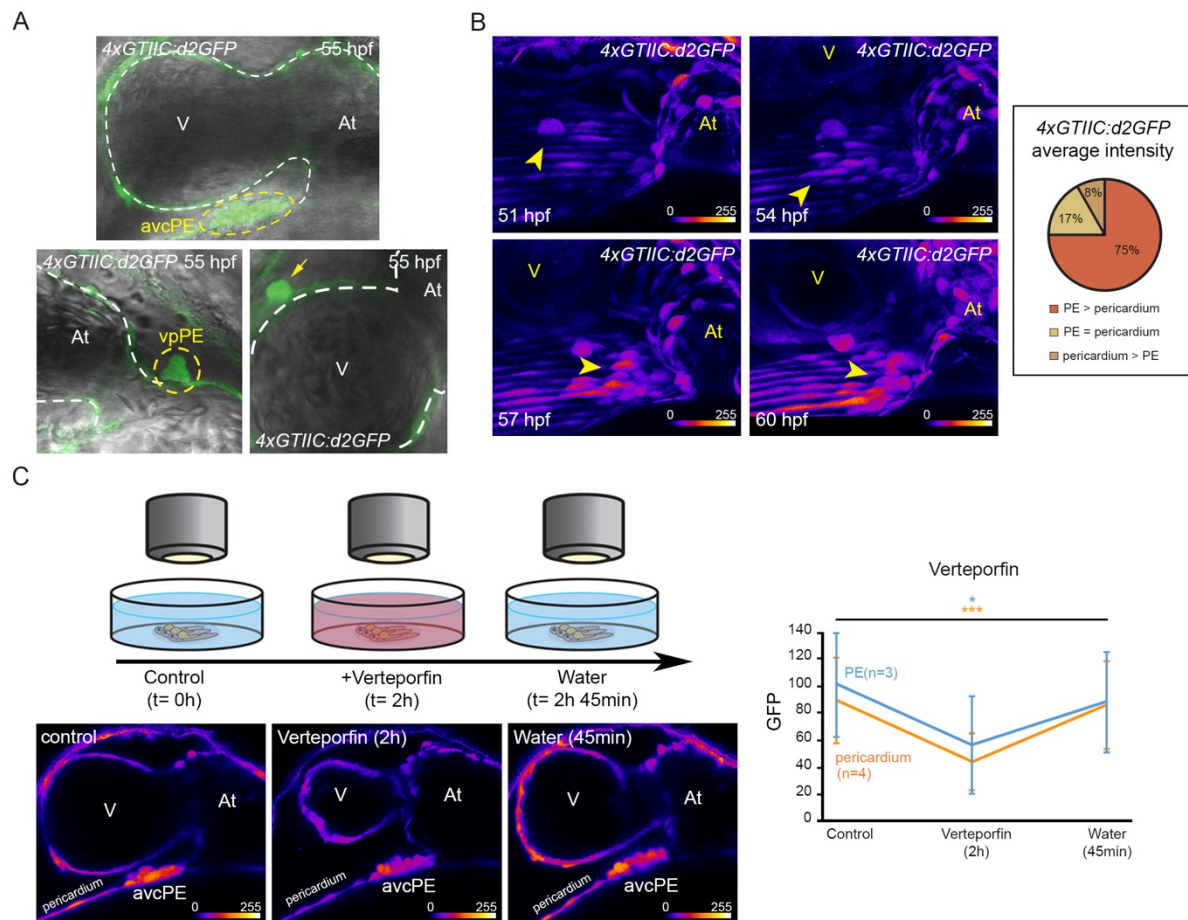
(A,B) *Ift20* and *Ift88* KO mice show left-right patterning defects including heart looping defects at E9.5. **(C)** Control and *Ift20* KO cryosections imaged by confocal microscopy after labelling with anti-TBX18 (white), anti-Arl13b (red) and anti- γ -tubulin (yellow) antibodies and Hoechst (blue) at E9.5. Zoomed region (enclosed in yellow box) shows the lack of Arl13b signal in *Ift20* KO mice. Individual channels are shown for Arl13b (red), γ -tubulin (yellow). **(C')** Control and *Ift88* KO cryosections labelled with anti-TBX18 (white), anti-Arl13b (red) and anti- γ -tubulin (yellow) antibodies and Hoechst (blue) at E9.5. Zoomed region (enclosed in yellow box) shows the decrease of Arl13b signal in *Ift88* KO mice. Individual channels are shown for Arl13b (red), γ -tubulin (yellow). **(C'')** Graph shows the percentage of ciliated PE cells in *Ift20* KO ($n=3$, *Ift88* KO ($n=3$) and control ($n=3$) mice. The percentage of ciliated PE cells is severely reduced in *Ift20* KO ($n=3$) and *Ift88* KO ($n=3$) when compared to control ($n=3$) mice. (t-test *Ift20* p -value 0.024; t-test *Ift88* p -value 0.025) **(D)** Control and *Ift88* KO cryosections labelled with WT1 (red), p -smad 1/5/9 (yellow) and Hoechst (blue) at E9.5. Individual channel is displayed for p -smad 1/5/9 as ice LUT to facilitate the visualization of signal intensity (green is the minimum and red is the maximum). Graph shows that the percentage of p -smad 1/5/9 positive PE cells is similar in *Ift88* KO ($n=3$ embryos: 1477 nuclei analyzed) and controls ($n=3$ embryos: 1514 nuclei analyzed) (Chi-square test of homogeneity =0.15225, p -value 0.6964 on 1 degree of freedom).



Supplementary Figure 4. *bmp4* is overexpressed in *ift88*, *elipsa/ift54* and *Ift20* mutants.

(A) The top two graphs show total myocardial and atrial-myocardial cell numbers quantified in *ift88* ($n=13$) mutants and controls ($n=14$) at 55 hpf. (t -test total myocardium p -value 0.016; atrial myocardium p -value 0.003). The bottom two graphs show total myocardial and atrial-

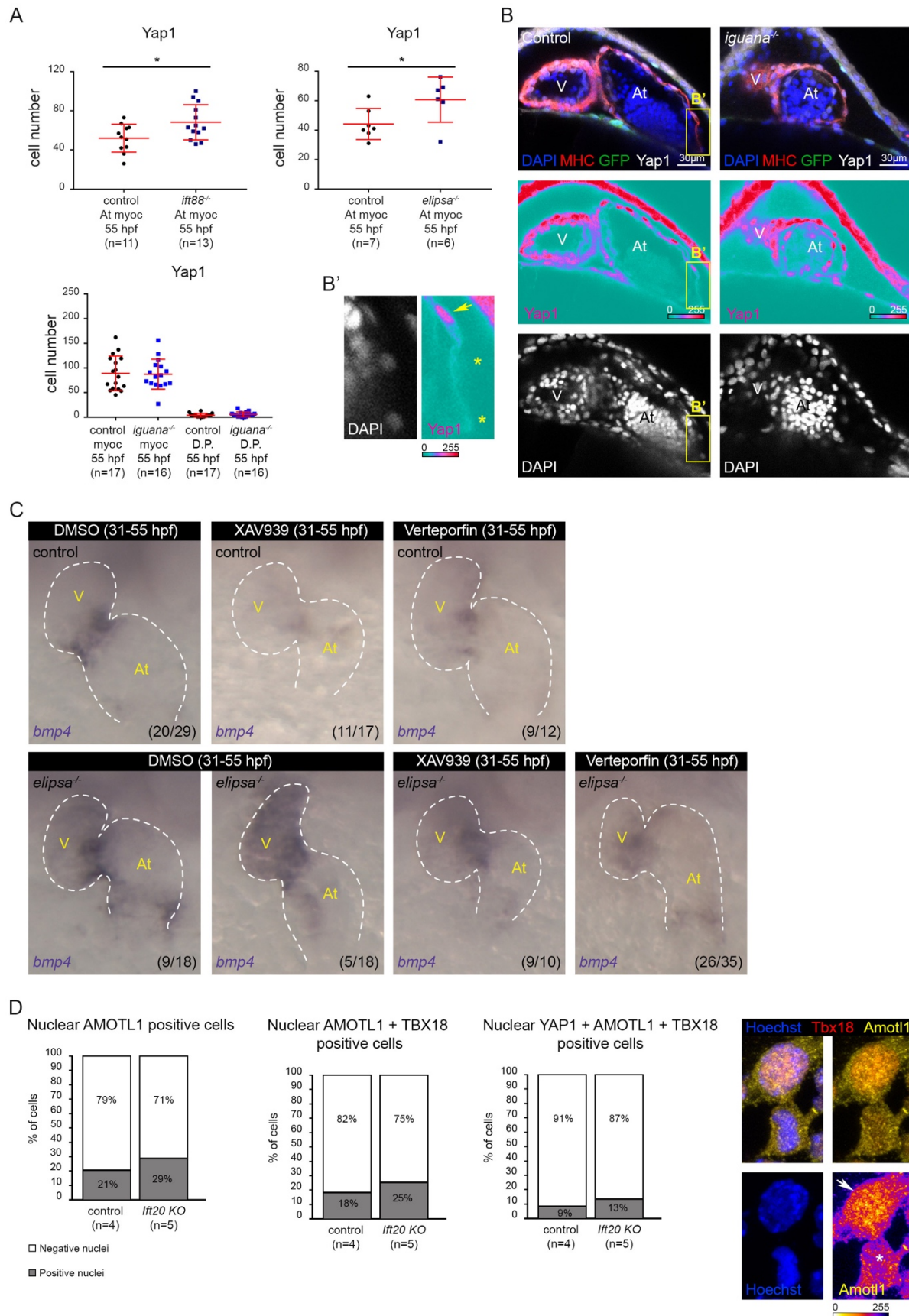
599 myocardial cell number quantified in iguana (n=24) mutants and controls (n=18) at 55 hpf. (t-
600 test total myocardium p-value 0.2; atrial myocardium p-value 0.68). **(B)** Whole mount *bmp4* in
601 situ hybridization performed on control and *ift88* mutant embryos at 48 hpf and at 55 hpf on
602 *ift88*, *elipsa* and *iguana* mutants and their controls. Yellow arrows point to *bmp4*
603 overexpression, while white asterisks mark reduced or absent expression. Ventral views,
604 anterior is to the top. V, ventricle; At, atrium. **(C)** Graphs show number of *p-smad1/5* positive
605 cells in the atrial myocardium quantified in *ift88* (at 50 hpf n=8; at 55 hpf n=7), *elipsa* (n=14)
606 mutants and their controls (n=7; n=5; n=10 respectively). At 50 hpf, *ift88* mutants show *p-*
607 *smad 1/5* increased cell number on the atrial myocardium (t-test p value 0.0017). Similar data
608 were obtained at 55 hpf (t-test p value 0.0008). At 55 hpf, *elipsa* mutants also show *p-smad 1/5*
609 increased cell number in the atrial myocardium (t-test p value 0.0003). At 55 hpf, *ift88* mutants
610 show *p-smad 1/5* increased cell numbers in the myocardium (t-test p value 0.005). **(D)** 3D
611 projections of whole mount immunofluorescence of hearts using anti-myosin heavy chain
612 antibody (MHC) (red), *epi:GFP* (green) and anti-*p-smad1/5* (yellow) antibody. Arrows mark
613 *avcPE* cells positive for *epi:GFP* and *p-smad1/5*. Zoomed confocal sections show *avcPE* in
614 *ift88* mutant and control embryos. Individual channels are displayed for *p-smad 1/5* and *GFP*.
615 Ventral views, anterior is to the top. In all graphs, red bars indicate mean \pm standard deviation.



Supplementary Figure 5 Yap1-Tead activity during proepicardial development in zebrafish.

(A) Confocal sections of 4xGTIIC:d2GFP signal merged with bright-field, showing Yap/Wwtr1-Tead interaction in avcPE, vpPE, epicardial, myocardial and pericardial cells (n=12). Yellow dashed circles enclose the avcPE and the vpPE. Arrow shows an epicardial cell. Ventral views, anterior is to the top. **(B)** Maximum projection 4xGTIIC:d2GFP time lapse (51-60 hpf) snapshots (n=6). Arrowheads point at the avcPE. GFP signal is shown as fire LUT where blue is the minimum and yellow is the maximum to facilitate visualization of the intensity changes through the experiment. Ventral views, anterior is to the top. V, ventricle; At, atrium. Graph shows 75% of the embryos displayed higher average GFP intensity in PE cells than in pericardial cells (n=12, 7-15 cells of each type). **(C)** Scheme of the experiment to assess Verteporfin specificity. Time lapse performed on 4xGTIIC:d2GFP embryos at 55 hpf. Yap/Wwtr1-Tead activity (average GFP intensity) was measured on the same PE (3 cells in

629 *each embryo, n=3) and pericardial (3 cells in each embryo, n=4) cells at three timepoints:*
630 *before adding Verteporfin (5 μ M) (t=0h), after 2 hours of treatment (t=2h) and 45 min after*
631 *washing out the Verteporfin with fish water (t=2h45 min). Graph shows the decrease in*
632 *Yap/Wwtr1-Tead activity (average GFP intensity) due to Verteporfin treatment on PE (blue)*
633 *and pericardial (orange) cells, which is rescued after removing the inhibitor. (Pericardial cells*
634 *ANOVA p value 0.0007. PE cells ANOVA p value 0.05). Example of 4xGTIIC:d2GFP embryo*
635 *confocal sections used for the experiment. GFP signal is shown as fire LUT where blue is the*
636 *minimum and yellow is the maximum to facilitate visualization of the intensity changes through*
637 *the experiment. Ventral views, anterior is to the top. V, ventricle; At, atrium.*



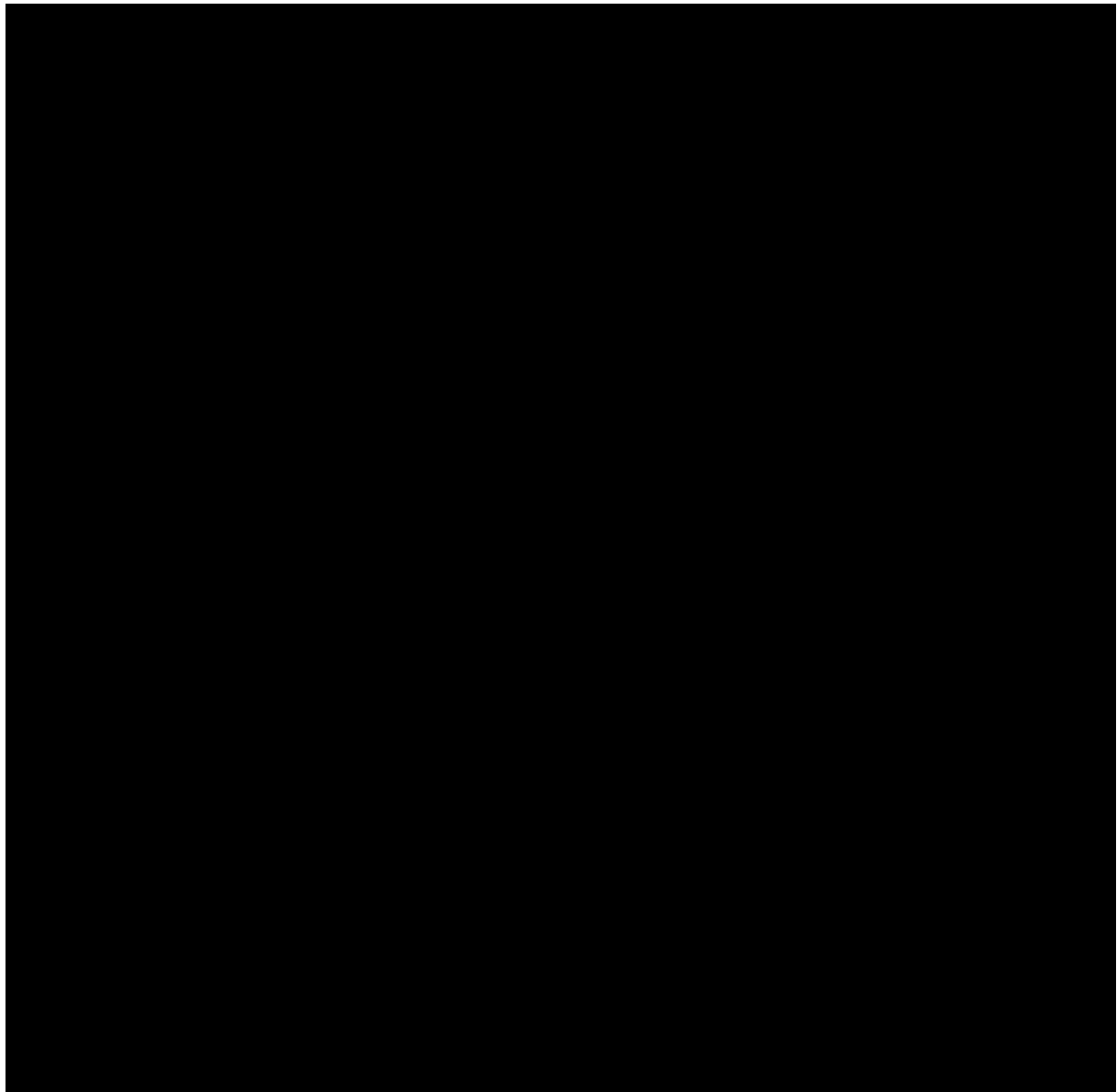
Supplementary Figure 6. Yap1 activity is increased in the myocardium of *ift88* and *elipsa/ift54* zebrafish mutants and *AMOTL1* activity is increased in *IFT20* KO mice proepicardium

(A) The top two graphs show number of Yap1-positive cells in the atrial myocardium quantified in *ift88*^{-/-}, *epi:GFP* (n=13) and *elipsa*^{-/-}, *epi:GFP* (n=6) mutants and their controls (n=11 and n=7 respectively) at 55 hpf. Mutants show increased Yap1-positive cell numbers (t-test *ift88* p value 0.024 and *elipsa* p value 0.042). Bottom graph shows number of Yap1-positive cells in the myocardium and dorsal pericardium (D.P.) quantified in *iguana*^{-/-}, *epi:GFP* (n=16) mutants and their controls (n=17) at 55 hpf (t-test myocardium p value 0.875 and D.P. p value 0.312).

(B) Control and *iguana*^{-/-}, *epi:GFP* immunofluorescence confocal sections labelled with anti-myosin heavy chain antibody (MHC) (red), GFP (green), anti-Yap1 antibody (white) and DAPI (blue) at 55 hpf. Individual channel is displayed for Yap1 (signal is shown as ice LUT to facilitate visualization of signal intensity, where green is the minimum and red is the maximum) and DAPI (white). Ventral view, anterior is to the top. **(B')** Zoomed region (yellow box in panel **B**) shows Yap1 and DAPI channels to illustrate the method used to quantify Yap1-positive (Yap1 signal in the nucleus: yellow arrow) and -negative (yellow asterisks) cells. **(C)** Whole mount *bmp4* in situ hybridization in untreated *elipsa* mutant (n=18) and control (n=29) embryos and treated with XAV939 (10μM) (*elipsa* mutant, n=10 and control, n=17) or Verteporfin (20μM) (*elipsa* mutant, n=35 and control, n=12) from 31 to 55 hpf. Treated embryos showed either decreased or absent *bmp4* expression at the atrioventricular canal myocardium and the venous pole. Ventral views, anterior is to the top. **(D)** Graphs show the percentages of *AMOTL1*-positive PE cells, double *AMOTL1*-*TBX18*-positive PE cells and triple *YAP1*-*AMOTL1*-*TBX18*-positive PE cells in *Ift20* KO (n=5 embryos: 1196 nuclei analyzed) and control (n=4 embryos: 929 nuclei analyzed) mice at E9.5. The percentage of nuclear *AMOTL1*-positive cells (Chi-square test of homogeneity = 14,748, p-value 1,23E-04 on 1 degree of freedom), nuclear

664 *AMOTL1-TBX18-positive cells (Chi-square test of homogeneity = 12,506, p-value 4,06E-04*
665 *on 1 degree of freedom) and nuclear YAP1-AMOTL1-TBX18-positive cells (Chi-square test of*
666 *homogeneity = 6,9059, p-value 8,59E-03 on 1 degree of freedom) were higher in Ift20 KO than*
667 *in control mice. Control (n=4) and Ift20 KO (n=5) sections labelled with TBX18 (red), Amotl1*
668 *(yellow) and Hoechst (blue). Individual AMOTL1 channel shows the difference between*
669 *nuclear AMOTL1-positive cells (white arrow) and AMOTL1-negative cells (white asterisk).*
670 *AMOTL1 signal is shown as fire LUT to facilitate visualization of the signal intensity, where*
671 *blue is the minimum and yellow is the maximum. In all graphs, red bars indicate mean*
672 *±standard deviation. V, ventricle; At, atrium.*

673



674

675 ***Supplementary Figure 7. IFT88-GFP co-localize with YAP1 in the cytoplasm.***

676 ***(A)*** Confocal section of HeLa cells transfected with IFT88-GFP and Yap1-Myc plasmids (48h).

677 DAPI (blue), IFT88-GFP (green) and Yap1 (visualized using anti-Myc antibody) (red).

678 Individual channels are displayed for IFT88-GFP and Yap1-Myc. ***(1-4)*** Zoom of selected areas

679 inside boxes showing co-localization. ***(B)*** Confocal sections of HeLa cells transfected with

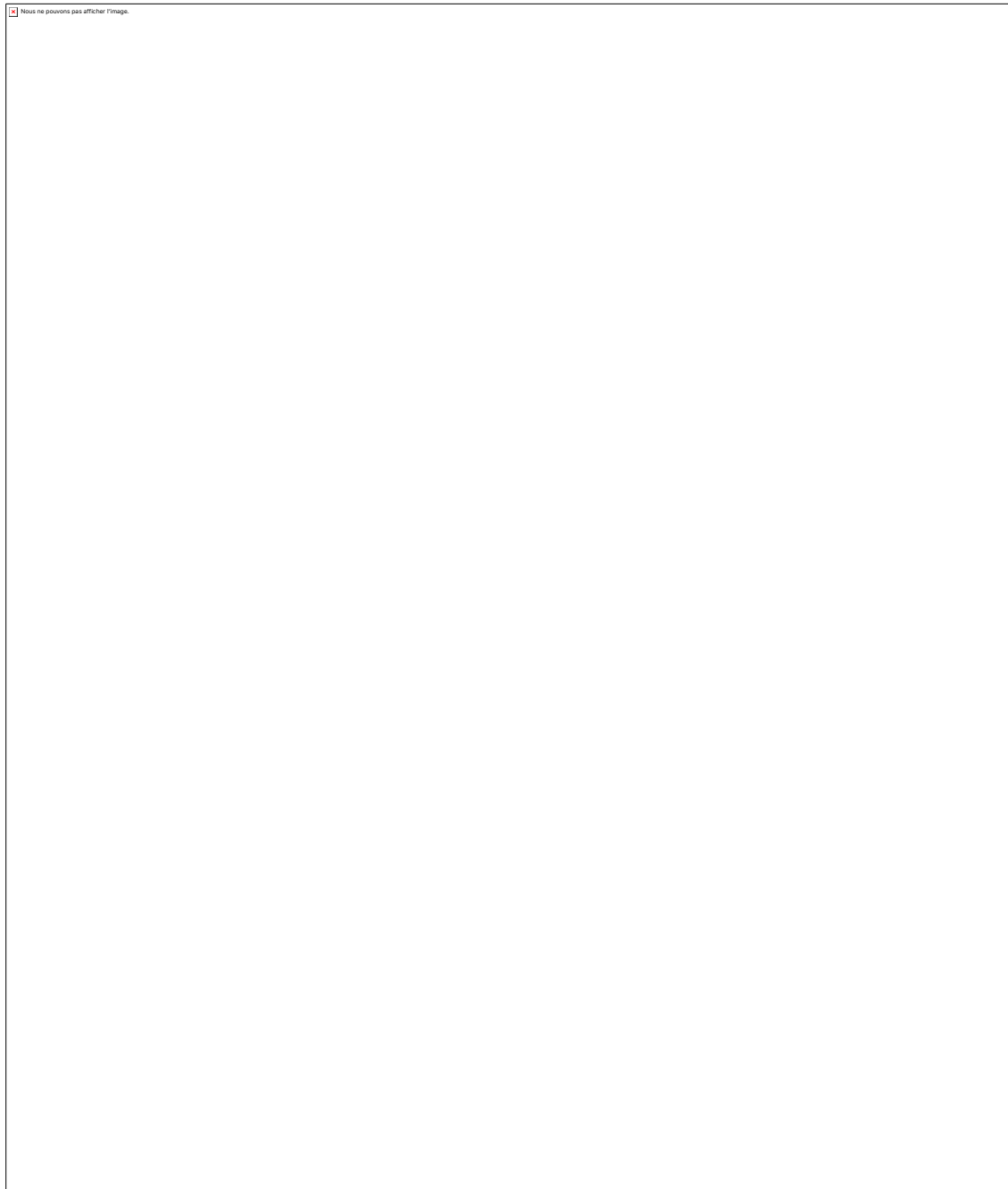
680 IFT88-GFP (48h) showing co-localization with endogenous YAP (visualized using anti-

681 YAP/WWTR1 (TAZ) antibody). DAPI (blue), IFT88-GFP (green) and YAP1 (magenta). ***(1-3)***

682 Zoom of the selected areas inside white boxes showing co-localization of IFT88 and YAP1.

683 Individual channels are displayed for IFT88-GFP and YAP1 signals. ***(C)*** Confocal sections of

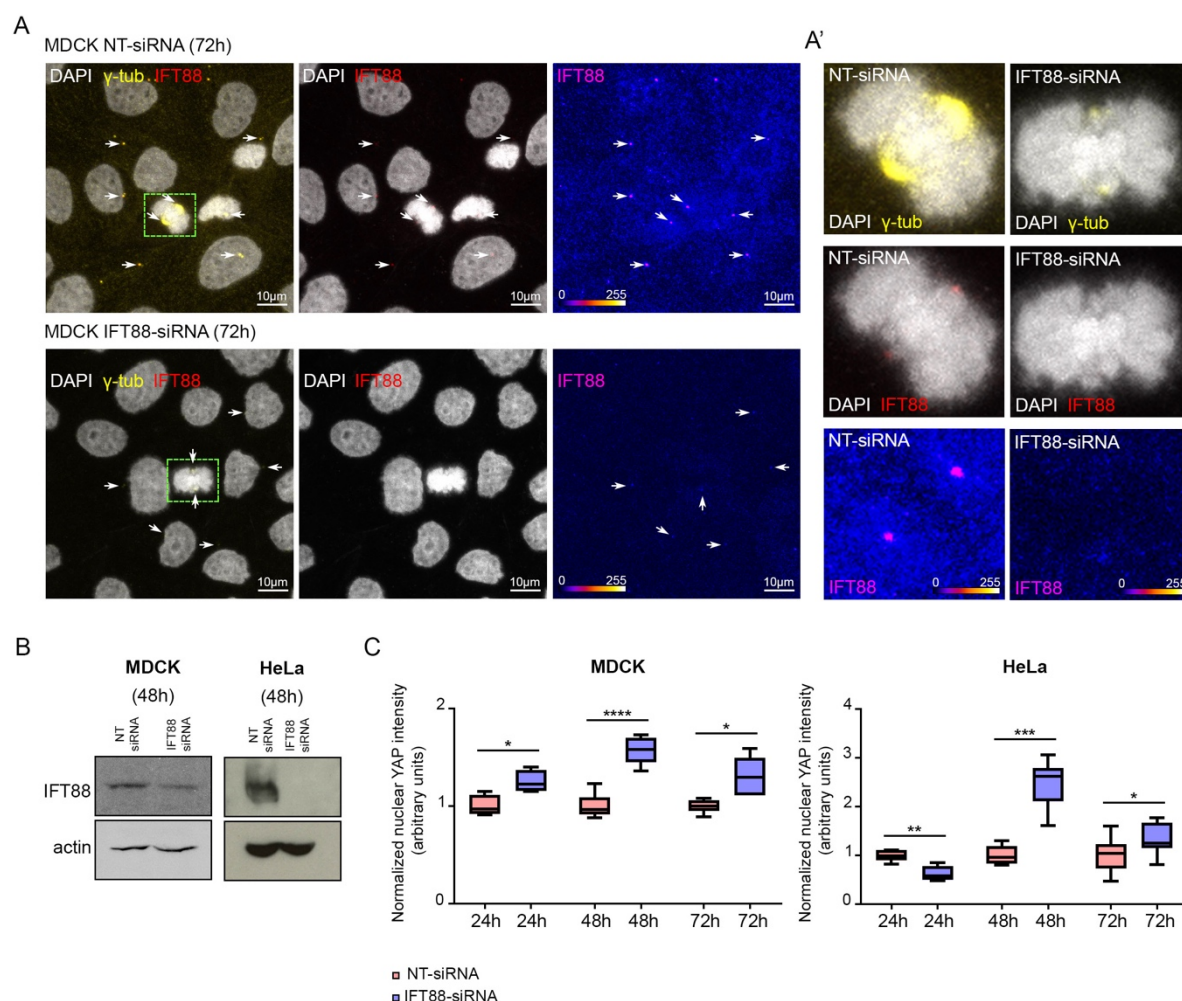
684 *HeLa cells transfected with Yap1-Myc (48h) showing co-localization with endogenous YAP1*
685 *(visualized using anti-YAP/WWTR1 (TAZ) antibody). DAPI (blue), Yap1-Myc (green) and*
686 *YAP1 (magenta). (1-3) Zoom of the selected areas inside white boxes showing examples of co-*
687 *localization between Yap1-Myc (visualized using anti-Myc antibody) and endogenous YAP1*
688 *(using YAP/WWTR1 (TAZ) antibody) signals. Individual channels are displayed for Yap1-Myc*
689 *and YAP1 signals. (D) Confocal sections of HeLa cells transfected with pEGFP C1 (48h) do*
690 *not show co-localization with endogenous YAP1 (visualized using anti-YAP/WWTR1 (TAZ)*
691 *antibody). DAPI (blue), pEGFP C1 (green) and YAP1 (magenta). Individual channels are*
692 *displayed for pEGFP C1 and YAP1 signals.*



Supplementary Figure 8. IFT88 and IFT20 regulate YAP1 activity.

(A) YAP1 Nuclear/cytoplasmic ratio is increased in cells treated with auxin (6h) (Mann-Whitney p -value 0.004). (controls: 2 replicates, $n=102$ cells; Auxin 6h: 2 replicates, $n=104$ cells). Immunofluorescence confocal images (z-projection) of DLD-1 cells treated with auxin (6 h) and controls. DAPI (blue), YAP1 (white) and α -tubulin (red). Zoomed regions show DAPI and YAP1 channels. YAP1 channel is shown in ice LUT where green is the minimum and red is the maximum to facilitate the visualization of signal intensity increases after treatment. **(B-D)**

IFT88 and IFT20 overexpression assays performed in HeLa cells (48h). Graphs show nuclear YAP/WWTR1 (TAZ) signal in GFP-positive cells (+ GFP), compared to GFP-negative cells (- GFP: endogenous control) in cells transfected with pEGFP C1 (GFP control) (n=4 replicates, average cell number analyzed for each condition = 22, t-test p-value 0.5) (B), IFT88-GFP (n=3 replicates, average cell number analyzed for each condition = 23, t-test p-value 0.01) (C) or IFT20-GFP (n=4 replicates, average cell number analyzed for each condition = 27, t-test p-value 0.03) (D). Box and whiskers (5-95 percentile). Outliers are represented as red dots (- GFP) or blue squares (+GFP). Immunofluorescence confocal images (z-projection) of cells transfected with pEGFP C1 (GFP control), IFT88-GFP or IFT20-GFP. DAPI (blue) and YAP/WWTR1 (TAZ) (white). Yellow arrows mark GFP signal.



Supplementary Figure 9. Efficiency validation of IFT88-siRNA in MDCK and HeLa cells.

(A) Immunofluorescence microscopy images (maximum projection) of MDCK cells treated with NT- or IFT88-siRNA (72h). DAPI (white), γ -tubulin (yellow) and IFT88 (red). White arrows highlight IFT88-positive centrosomes facilitating the visualization of IFT88 signal depletion upon IFT88-siRNA treatment. (A') Zoom of dividing cells (green boxes) treated with NT-siRNA and IFT88-siRNA respectively. Centrosomes show reduced IFT88 (red) and γ -tubulin (yellow) signal after IFT88 depletion. DAPI (white). IFT88 channel is shown in fire LUT where blue is the minimum and yellow is the maximum to facilitate the visualization of the intensity reduction after the treatment. (B) Western blot analysis of HeLa and MDCK cells after 48h NT- and IFT88-siRNA treatments respectively. (C) Graphs show the increase in nuclear YAP/WWTR1 (TAZ) signal in IFT88-siRNA treated cells (blue), compared to NT-siRNA controls (red) at 24,

48 and 72h. Box and whiskers (5-95 percentile). (MDCK: 24h: n=1 replicate, average cell number analyzed for each condition = 42, t-test p-value 0.02; 48h: n=1 replicate, average cell number analyzed for each condition = 52, t-test p-value <0.0001; 72h: n=1 replicate, average cell number analyzed for each condition = 126, t-test p-value 0.01) (HeLa: 24h: n=1 replicate, average cell number analyzed for each condition = 12, t-test p-value 0.001; 48h: n=1 replicate, average cell number analyzed for each condition = 12, t-test p-value 0.0002; 72h: n=1 replicate, average cell number analyzed for each condition = 32, t-test p-value 0.047).

Average intensity	Embryo_01	Embryo_02	Embryo_03	Embryo_04	Embryo_05	Embryo_06
PE cells	71,37	72,42	30,84	89,57	69,72	49,63
St-Dev	11,91	21,49	26,85	20,56	24,85	13,35
Pericardial cells	52,45	45,17	55,81	94,08	49,98	29,95
St-Dev	21,16	9,76	18,25	29,84	14,67	7,51
t-test	0,0325	0,0084	0,0101	0,7309	0,0608	0,0001

Average intensity	Embryo_07	Embryo_08	Embryo_09	Embryo_10	Embryo_11	Embryo_12
PE cells	63,69	60,99	115,45	64,67	56,23	107,03
St-Dev	26,92	18,28	6,52	11,43	10,46	21,14
Pericardial cells	28,76	31,59	74,03	36,44	30,05	68,40
St-Dev	16,68	7,78	22,14	6,82	8,85	28,52
t-test	0,0055	0,0005	0,0001	0,0000	0,0002	0,0024

741 *Supplementary Table 1. Yap/Wwtr1-Tead activity (GFP average intensity) in PE and*
 742 *pericardial cells.*

743

744 *Movie 1. Multiple avcPE clusters in ift88 mutant.*

745

746 *Movie 2. Immotile and bent cilia protruding from the avcPE.*

747

748 *Movie 3. Absence of avcPE cluster in iguana mutant.*

749

750 *Movie 4. Yap/Wwtr1-Tead activity during avcPE development (51-60 hpf).*

751

752 *Movie 5. 3D projection of the PE (marked by anti-Wt1 antibody) of a control embryo at E*
 753 *9.5.*

754

755 *Movie 6. 3D projection of the PE (marked by anti-Wt1 antibody) of a IFT20 KO embryo at E*
 756 *9.5.*

757

758

759

Material and Methods

Zebrafish (ZF) husbandry and embryo treatments:

Animal experiments were approved by the Animal Experimentation Committee of the Institutional Review Board of the IGBMC. ZF lines used in the study were *Et(-26.5Hsa.WT1-Igata2:EGFP)^{cn1}* transgenic line (referred to as *epi:GFP*) (46), *amotl2a^{fu46}* (33), *elipsa^{tp49d}* (10), *ift88^{tz288/oval}* (53), *iguana^{ts294e}* (54), *yap1^{fu48}* (33), *4xGTIIC:d2GFP* (61), *actb2:Mmu.Arl13b-GFP* (56) and *tcf21:NLS-EGFP* (87). All animals were incubated at 28.5°C for 24h before treatment with 1-phenyl-2-thiourea (PTU) (Sigma Aldrich) to prevent pigment formation.

Verteporfin (Sigma Aldrich) was diluted to 5 µM in fish tank water with 0.0033% PTU, in which larvae were incubated in darkness for 5h at 28.5°C.

ZF Immunofluorescence:

Embryos were fixed at the desired stages in 4% paraformaldehyde (PFA) overnight at 4°C. After washing in 0.1% PBS Tween 20, embryos were permeabilized in 0.5% PBS Triton X-100 for 20 min at room temperature (RT). Samples were washed and then blocked (3% albumin from bovine serum (BSA), 5% goat serum, 20 mM MgCl₂, 0.3% Tween 20 in PBS) during 2h at RT. Primary antibodies were added in the blocking solution and incubated overnight at 4°C. Secondary antibodies were added in 0.1% PBS Tween20 after thorough washing and incubated overnight at 4°C. Embryos were washed and incubated with DAPI (Invitrogen), 1:1000, for 15 min at RT. After being thoroughly washed, samples were mounted for imaging on a Leica SP8 confocal with a dipping immersion objective (Leica HCX IRAPO L, 25X, N.A. 0.95). Z-stacks were taken every 10 µm. 3D images were reconstructed using IMARIS software (Bitplane Scientific Software). The ventral pericardium was digitally removed to provide a clearer view of the heart.

Antibodies used were as follows: anti-myosin heavy chain (MF20, DSHB) 1:20, anti-GFP (AVES) 1:500, anti-phospho-Smad 1/5 (Ser463/465) (Cell signaling) 1:50, anti-Yap1 (Lecaudey lab) 1:200. Secondary antibodies: goat anti-chicken Alexa Fluor 488 IgY (H+L) (Invitrogen), goat anti-mouse IgG Cy3 conjugate (H+L) (Life technologies) and goat anti-rabbit Alexa Fluor 647 (ThermoFisher) were used at 1:500.

To test the effects of Verteporfin treatment, embryos were rinsed in fish tank water before being fixed and processed as described above.

avcPE cell quantification:

We performed whole-mount immunofluorescent staining on control and mutant embryos in the *epi:GFP* reporter line background and imaged the heart using a confocal microscope with a z-step of 10 μ m. The different tissues were labeled using anti-myosin heavy chain (MHC) (myocardium) and anti-GFP (*epi:GFP*) antibodies, and DAPI dye to stain for nuclei. We then manually quantified the number of avcPE cells per z slice. We identified the avcPE clusters anatomically: avcPE clusters form in the dorsal pericardium, close to the atrio-ventricular canal (avc). PE cells were identified by their rounded morphology in conjunction with their expression of GFP (although some pericardial cells are also GFP-positive, they can be excluded due to their flat morphology). In order to count each cell only once in the z-stack, we only counted a cell when its nucleus was visible.

Myocardial cell quantification:

We performed whole-mount immunofluorescent staining on control and mutant embryos using anti-myosin heavy chain (MHC) (myocardium) antibody and DAPI dye (nuclei). We imaged the heart using a confocal microscope with a z-step of 10 μ m. We then manually quantified the number of myocardial cells per z slice (nuclei surrounded by MHC signal).

In situ hybridization (ISH):

ISH was performed in whole embryos according to (Thisse and Thisse, 2008) with minor modifications. Antisense mRNA probe used was against full coding sequence of *bmp4*.

In vivo imaging:

ZF embryos were staged, anaesthetised with 0.02% tricaine solution and mounted in 0.7% low melting-point agarose (Sigma Aldrich). Confocal imaging was performed on a Leica SP8 confocal microscope. Images were acquired bidirectionally with a low-magnification water immersion objective (Leica HCX IRAPO L, 25X, N.A. 0.95). For time lapse, z-stacks were acquired each 15 or 30 min, depending on the experiment. The optical plane was moved 15 µm between z-sections.

Bright field experiments were performed on a Leica DMIRBE inverted microscope using a Photron SA3 high speed CMOS camera (Photron, San Diego, CA) and water immersion objective (Leica 20X, NA 0.7). Image sequences were acquired at a frame rate of 150 frames per second.

Mouse models:

Ift20^{null/+} (88) and *Ift88^{null/+}* (89) mice were maintained on a C57BL/6JRj and B6D2 genetic background respectively. Animal procedures were approved by the ethical committee of the Institut Pasteur and the French Ministry of Research. E9.5 embryos were isolated in 200ng/ml cold heparin, incubated in cold 250mM KCl and fixed in 4% paraformaldehyde in PBS inside a rotative oven at 37°C overnight to remove excess of blood. Male and female samples were mixed.

Whole mount immunofluorescence in the mouse:

Embryos were fixed in paraformaldehyde. The cardiac region was dissected, permeabilised in 0.75% Triton. Aldehydes were quenched with 2.6mg/ml NH₄Cl. Immunostaining was performed in 10% inactivated horse serum, 0,5% Triton with a primary antibody against Wt1

(Santa Cruz sc-192, 1:50), and with Alexa Fluor conjugated secondary antibodies (1:300) and counterstained with Hoechst (1 :400). 80% glycerol was used to make the samples transparent.

Mice PE volume analysis:

Whole mount embryos stained with Wt1 antibody (Santa Cruz) were scanned on TCS SP8 DLS (Digital Light Sheet) Leica with a water immersion objective (HC APO L, 10X, 0.3). Z-stacks were taken every 2 μ m. Both, coronal and sagittal views were acquired, if possible, for a more precise analysis. **(Supp. 2 F)** Using Matlab software, the contour of the PE was manually drawn (Wt1 signal) for each z plane and the area (A) was calculated. Volume (V) was estimated as:

$$V = \sum_{i=1}^n A_i \times dz ; \quad i=1 ; \quad n=\text{number of planes}; \quad dz= 2 \mu\text{m}$$

3D images were reconstructed using IMARIS software (Bitplane Scientific Software).

Immunofluorescence on cryosections in the mouse:

Embryos were embedded in 7% gelatin, 15% sucrose, frozen in cold isopentane and sectioned on a cryostat (10 μ m). Immunostaining was performed on cryosections as described above, with permeabilisation in 0.5% Triton, and with an additional incubation in 0.2 mg/mL goat anti-mouse IgG Fab fragment to reduce non-specific reactivity of antibodies raised in the mouse. Primary antibodies against Tbx18 (Santa Cruz sc-17869, 1:100), Wt1 (Santa Cruz sc-192, 1:50), Yap1 (Santa Cruz sc-101199, 1:100), Amotl1 (Sigma HPA001196, 1:50) and p-Smad1/5/9 (Cell signaling 13820, 1:250) were used, with Alexa Fluor conjugated secondary antibodies (1:500) and Hoechst nuclear counterstaining (1:1000). Samples were imaged in DAKO mounting medium on a LSM700 (Zeiss) confocal microscope with a 40X/1.3 objective. Z-stacks were taken every 0.9 μ m.

Yap1- and Amotl1-positive cell quantifications:

Nuclei positions on the slides were defined using IMARIS (Bitplane Scientific Software) Spots detection function. The results were manually corrected if needed. Nuclei positions were exported from Imaris and imported to Matlab. Each cell was assigned a unique index. The

intensity of Tbx18 signal was evaluated in correspondence with the nuclei positions. Cells where the intensity was found higher than a threshold were considered positive. The threshold was established according to the background noise intensity. Results were manually corrected if needed and Tbx18-positive cells were automatically counted. Yap1 signal was visualized in fire LUT to facilitate perception of signal intensity. Nuclear Yap1-positive cells (higher signal in the nucleus than in the cytoplasm) were manually defined through index identification of cells and counted automatically. The same procedure was followed for Amotl1 signal. The outline of the outer PE region was manually drawn and areas of the two regions were calculated automatically. Matlab provided the total positive cell number for each signal and area, including signal co-localization (**Supp. 3 E**).

Cell culture, siRNAs and transfection:

Cells were cultured in appropriate conditions: MDCK (MEM Eagle - Earle's BSS, 10 % FCS, AANE 0.1 mM, Sodium Pyruvate 1mM, Gentamicin 40 µg/ml), HeLa (DMEM 4.5 g/l glucose, 10% FCS, Penicillin 100 UI/ml, Streptomycin 100 µg/ml), HEK293 cells (DMEM 1g/L glucose, FCS 10%, Penicillin 100 UI/ml, Streptomycin 100 µg/ml) and DLD-1 (DMEM 4.5 g/l glucose, 10% FCS, Penicillin 100 UI/ml, Streptomycin 100 µg/ml) siRNA (Dharmacon) ON-Target plus - Control pool Non-targeting (D-001810-10-05) and SMART pool human IFT88 (L-012281-01) were used at 50 nM working concentration. Cells were transfected 16h after splitting using Opti-MEM medium and Oligofectamine reagent.

Generation of DLD-1 IFT88-AID targeted cells:

DLD-1 IFT88-AID cells were generated by adding an AID tag followed by a YFP tag at the 3' end of the last exon on the IFT88 genomic locus. In detail, a clonal population of DLD-1 cells stably expressing TIR1-9xMyc protein was used for targeting (90). sgRNA targeting two regions adjacent to the 3' end of IFT88 gene were introduced under the control of U6 transcription promoter into two separate vectors encoding for the expression of the Cas9 nickase

(D10A) (91) (addgene 42335). A donor construct containing ≈ 600 bp recombination arms surrounding the 3' end of IFT88 locus, in frame with a sequence encoding for an AID-YFP-Stop sequence, was generated. All three vectors were transfected into DLD-1 TIR1 cells using Xtreme Gene 9 DNA transfection reagent (Roche). Cells were sorted based on their YFP fluorescence and single clones were isolated. Homozygous targeted clones were identified by PCR. Targeting of IFT88 and degradation of IFT88-AID-YFP was confirmed by immunoblot following addition of Auxin (Sigma-Aldrich) at 500 μ M in the culture medium for the indicated times.

Immunofluorescence on cells:

Cells were fixed in 100% MeOH for 6 min at -20°C (Ift88 and γ -tubulin antibodies), in 4% PFA for 7 min at RT (DLD-1 cells. Yap1 antibody) or in PFA 4% for 17 min at RT (MDCK and HeLa cells. Yap/Taz antibody). After washing in 0.1% PBS Tween20, cells were permeabilized in 0.5% PBS-NP40 and blocked in 5% BSA 1h at RT. Primary antibodies were added in the blocking solution and incubated overnight at 4°C. Secondary antibodies were added in 0.1% PBS Tween20 after washing and incubated for 2h at RT. Then cells were incubated with DAPI (Invitrogen), 1:1000, for 15 min at RT. After being thoroughly washed, samples were mounted for imaging on a Leica SP5 (siRNA experiments) or SP8 (DLD-1 experiments and experiments to assess subcellular localization) confocal microscope with an oil immersion objective (Leica HCX PL APO lambda blue, 63X, N.A. 1.4). Z-stacks were taken every 1 μ m.

Antibodies used were as follows: anti- γ -tubulin (Santa Cruz) 1:500, anti- α -tubulin (Sigma, 1:2000), anti-IFT88 (Euromedex) 1:50, anti-Yap1 (4912) (Cell signaling) 1:50 (DLD-1 experiments), and anti-Yap/Taz (D24E4) (Cell signaling) 1:50 (MDCK and HeLa siRNA experiments). Secondary antibodies: goat anti-mouse IgG Cy3 conjugate (H+L) (Life technologies) and goat anti-rabbit Alexa Fluor 647 (In vitrogen) were used at 1:500.

Nuclear Yap quantifications:

Analyses were performed using Image J. Nuclei areas were selected manually using DAPI signal as reference on z-projection images (sum slices for DLD-1 experiment and maximum intensity projection for siRNA experiments). Yap average nuclear signal intensity was measured for the selected areas. In experiments in DLD-1 cells the values were measured for each individual nucleus, while in the case of siRNA experiments, all the nuclei in a slice were measured together. Values were normalized to their controls in order to merge data from different experiments.

Nuclear/cytoplasmic Yap1 ratio:

Analyses were performed using Image J. Nuclei areas were selected manually using DAPI signal as reference on z-projection images (sum slices). Cytoplasmic areas were selected using α -tubulin signal as reference. Yap average nuclear signal intensity was measured for the nuclear ROI. Yap average cytoplasmic signal intensity was measured after subtracting nuclear ROI from the cytoplasmic ROI.

Lysates and immunoblotting:

DLD-1 cell extracts were obtained after lysis with Laemmli sample buffer of an equal number of cells for each sample. Proteins were resolved by SDS-PAGE, transferred to nitrocellulose membranes and revealed by immunoblot using Western Lightning Plus-ECL kit (PerkinElmer).

Immunoprecipitation (IP) assays:

HEK293 cells:

HEK293 cells (Q-BIOgene AES0503) were co-transfected with plasmids Flag-Amotl1 (92) and Ift20-GFP (9), or a Flag-control plasmid using Lipofectamine® 2000 Transfection Reagent (ThermoFisher SCIENTIFIC) and cultured for 48h. Proteins were extracted in a lysis buffer (10mM Tris-Cl pH 7.5, 5mM EDTA, 150mM NaCl, 10% glycerol and 5% CHAPS) in the presence of protease inhibitors (cOmplete™ Protease Inhibitor Cocktail, Roche). Immunoprecipitation of protein extracts was performed using a monoclonal anti-Flag antibody

covalently attached to agarose (Anti-FLAG M2 Affinity gel, Sigma). Proteins were eluted in 2xNuPAGE LDS Sample Buffer (ThermoFisher). Proteins were separated on SDS–polyacrylamide gel electrophoresis and transferred to a nitrocellulose membrane. Proteins were detected with the primary antibodies against Flag (1:1000, Sigma F7425), GFP (1:1000, ThermoFisher CAB421), Ift20 (1:500, Proteintech, 13615-1-AP), Yap1 (1:1000, Cell Signaling 4912S) and Amotl1 (1:1000, Sigma HPA001196), followed by HRP-conjugated secondary antibodies (1:5000, Jackson ImmunoResearch) and the ECL detection reagent.

HeLa cells:

We performed IPs using GFP-Trap (ChromoTek) agarose beads in two conditions: Control IP (YAP1-Myc (93), pEGFP-C1 and HA-Amotl1(23)) and IFT88 IP (YAP1-Myc, IFT88-GFP (94) and HA-Amotl1). HeLa cells (2x 10cm dish/ condition) were transfected with Lipofectamine 2000. Experiments were performed using the following setup: Cells were seeded at high density into 10cm dishes and transfected 16 hrs after seeding at 95% confluency. Twenty-four hours post-transfection, cells were seeded into 15cm dishes in order to achieve culture of isolated cells (10x 15cm dish/ condition). Proteins were extracted 60 hrs post-transfection in a lysis buffer (10mM TrisHCl, pH7.5; 150mM NaCl; 0.5mM EDTA; 0.5% NP-40; protease inhibitors Complete). GFP beads were washed once in lysis buffer and incubated with 16 mg of the protein lysate for 16 hrs at 4 °C. Beads were washed four times in buffer without detergent and proteins were eluted by boiling for 10 mins. The input (1%) and IP were analyzed using immunoblot and the membranes were probed with anti-GFP (Abcam), anti-Yap/TAZ (D24E4, Cell Signaling) and anti-HA (Sigma Aldrich) antibodies.

Statistics:

We applied D'Agostino & Pearson and Shapiro-Wilk normality tests to assess whether the samples fit a normal distribution and F test to compare variances. For normal distributed and homoscedastic samples, we used t-test or ANOVA. For non-parametric samples, we applied

Man-Whitney or Kruskal-Wallis. The pertinent statistical analyses for each experiment were performed using GraphPad Prism 7 software. For the analysis of nuclear p-smad 1/5/9 and YAP1 signal in mice we used the non-parametric Chi-squared test of homogeneity to test whether the observed frequency of positive nuclei was equally distributed across the *wild type* and mutant embryos.

1. Berbari NF, O'Connor AK, Haycraft CJ, Yoder BK. The Primary Cilium as a Complex Signaling Center. *Curr Biol* [Internet]. 2009 Jul 14 [cited 2018 Sep 6];19(13):R526–35. Available from: <http://www.ncbi.nlm.nih.gov/pubmed/19602418>
2. Reiter JF, Leroux MR. Genes and molecular pathways underpinning ciliopathies. *Nat Rev Mol Cell Biol* [Internet]. 2017 Jul 12 [cited 2018 Sep 6];18(9):533–47. Available from: <http://www.ncbi.nlm.nih.gov/pubmed/28698599>
3. Slough J, Cooney L, Brueckner M. Monocilia in the embryonic mouse heart suggest a direct role for cilia in cardiac morphogenesis. *Dev Dyn* [Internet]. 2008 Sep [cited 2018 Sep 6];237(9):2304–14. Available from: <http://www.ncbi.nlm.nih.gov/pubmed/18729223>
4. Li Y, Klena NT, Gabriel GC, Liu X, Kim AJ, Lemke K, et al. Global genetic analysis in mice unveils central role for cilia in congenital heart disease. *Nature* [Internet]. 2015 May 25 [cited 2018 Sep 6];521(7553):520–4. Available from: <http://www.ncbi.nlm.nih.gov/pubmed/25807483>
5. San Agustin JT, Klena N, Granath K, Panigrahy A, Stewart E, Devine W, et al. Genetic

- link between renal birth defects and congenital heart disease. Nat Commun [Internet].
2016 Mar 22 [cited 2018 Sep 6];7:11103. Available from:
<http://www.ncbi.nlm.nih.gov/pubmed/27002738>
6. Klena N, Gabriel G, Liu X, Yagi H, Li Y, Chen Y, et al. Role of Cilia and Left-Right
Patterning in Congenital Heart Disease [Internet]. Etiology and Morphogenesis of
Congenital Heart Disease: From Gene Function and Cellular Interaction to
Morphology. 2016 [cited 2018 Sep 6]. Available from:
<http://www.ncbi.nlm.nih.gov/pubmed/29787118>
7. Rosenbaum JL, Witman GB. Intraflagellar transport. Nat Rev Mol Cell Biol [Internet].
2002 Nov 1 [cited 2018 Sep 6];3(11):813–25. Available from:
<http://www.ncbi.nlm.nih.gov/pubmed/12415299>
8. Taschner M, Bhogaraju S, Lorentzen E. Architecture and function of IFT complex
proteins in ciliogenesis. Differentiation [Internet]. 2012 Feb [cited 2018 Sep
6];83(2):S12–22. Available from: <http://www.ncbi.nlm.nih.gov/pubmed/22118932>
9. Follit JA, Tuft RA, Fogarty KE, Pazour GJ. The Intraflagellar Transport Protein IFT20
Is Associated with the Golgi Complex and Is Required for Cilia Assembly. Margolis B,
editor. Mol Biol Cell [Internet]. 2006 Sep [cited 2018 Sep 6];17(9):3781–92. Available
from: <http://www.ncbi.nlm.nih.gov/pubmed/16775004>
10. Omori Y, Zhao C, Saras A, Mukhopadhyay S, Kim W, Furukawa T, et al. elipsa is an
early determinant of ciliogenesis that links the IFT particle to membrane-associated
small GTPase Rab8. Nat Cell Biol [Internet]. 2008 Apr 23 [cited 2018 Sep
6];10(4):437–44. Available from: <http://www.ncbi.nlm.nih.gov/pubmed/18364699>
11. Zhu X, Liang Y, Gao F, Pan J. IFT54 regulates IFT20 stability but is not essential for
tubulin transport during ciliogenesis. Cell Mol Life Sci [Internet]. 2017 Sep 17 [cited
2018 Sep 6];74(18):3425–37. Available from:

- 1007 <http://www.ncbi.nlm.nih.gov/pubmed/28417161>
- 1008 12. Pazour GJ, Dickert BL, Vucica Y, Seeley ES, Rosenbaum JL, Witman GB, et al.
1009 Chlamydomonas IFT88 and its mouse homologue, polycystic kidney disease gene
1010 tg737, are required for assembly of cilia and flagella. J Cell Biol [Internet]. 2000 Oct
1011 30 [cited 2018 Sep 6];151(3):709–18. Available from:
1012 <http://www.ncbi.nlm.nih.gov/pubmed/11062270>
- 1013 13. Hua K, Ferland RJ. Primary cilia proteins: ciliary and extraciliary sites and functions.
1014 Cell Mol Life Sci [Internet]. 2018 May [cited 2018 Sep 6];75(9):1521–40. Available
1015 from: <http://www.ncbi.nlm.nih.gov/pubmed/29305615>
- 1016 14. Vertii A, Bright A, Delaval B, Hehnly H, Doxsey S. New frontiers: discovering cilia-
1017 independent functions of cilia proteins. EMBO Rep [Internet]. 2015 Oct 1 [cited 2018
1018 Sep 6];16(10):1275–87. Available from:
1019 <http://www.ncbi.nlm.nih.gov/pubmed/26358956>
- 1020 15. Delaval B, Bright A, Lawson ND, Doxsey S. The cilia protein IFT88 is required for
1021 spindle orientation in mitosis. Nat Cell Biol [Internet]. 2011 Apr 27 [cited 2018 Sep
1022 6];13(4):461–8. Available from: <http://www.ncbi.nlm.nih.gov/pubmed/21441926>
- 1023 16. Taulet N, Vitre B, Anguille C, Douanier A, Rocancourt M, Taschner M, et al. IFT
1024 proteins spatially control the geometry of cleavage furrow ingression and lumen
1025 positioning. Nat Commun [Internet]. 2017 Dec 4 [cited 2018 Sep 13];8(1):1928.
1026 Available from: <http://www.nature.com/articles/s41467-017-01479-3>
- 1027 17. Robert A, Margall-Ducos G, Guidotti J-E, Bregerie O, Celati C, Brechot C, et al. The
1028 intraflagellar transport component IFT88/polaris is a centrosomal protein regulating
1029 G1-S transition in non-ciliated cells. J Cell Sci [Internet]. 2007 Feb 15 [cited 2018 Sep
1030 6];120(4):628–37. Available from: <http://www.ncbi.nlm.nih.gov/pubmed/17264151>
- 1031 18. Finetti F, Paccani SR, Riparbelli MG, Giacomello E, Perinetti G, Pazour GJ, et al.

- 1032 Intraflagellar transport is required for polarized recycling of the TCR/CD3 complex to
1033 the immune synapse. *Nat Cell Biol* [Internet]. 2009 Nov 25 [cited 2018 Sep
1034 6];11(11):1332–9. Available from: <http://www.ncbi.nlm.nih.gov/pubmed/19855387>
- 1035 19. Galgano D, Onnis A, Pappalardo E, Galvagni F, Acuto O, Baldari CT. The T cell
1036 IFT20 interactome reveals new players in immune synapse assembly. *J Cell Sci*
1037 [Internet]. 2017 Feb 2 [cited 2018 Sep 6];130(6):jcs.200006. Available from:
1038 <http://www.ncbi.nlm.nih.gov/pubmed/28154159>
- 1039 20. Xin M, Kim Y, Sutherland LB, Qi X, McAnally J, Schwartz RJ, et al. Regulation of
1040 Insulin-Like Growth Factor Signaling by Yap Governs Cardiomyocyte Proliferation
1041 and Embryonic Heart Size. *Sci Signal* [Internet]. 2011 Oct 25 [cited 2018 Sep
1042 17];4(196):ra70–ra70. Available from: <http://www.ncbi.nlm.nih.gov/pubmed/22028467>
- 1043 21. Fukui H, Miyazaki T, Chow RW-Y, Ishikawa H, Nakajima H, Vermot J, et al. Hippo
1044 signaling determines the number of venous pole cells that originate from the anterior
1045 lateral plate mesoderm in zebrafish. *Elife* [Internet]. 2018 May 29 [cited 2018 Sep 6];7.
1046 Available from: <https://elifesciences.org/articles/29106>
- 1047 22. Lai JKH, Collins MM, Uribe V, Jiménez-Amilburu V, Günther S, Maischein H-M, et
1048 al. The Hippo pathway effector Wwtr1 regulates cardiac wall maturation in zebrafish.
1049 *Development* [Internet]. 2018 May 15 [cited 2018 Sep 6];145(10):dev159210.
1050 Available from: <http://www.ncbi.nlm.nih.gov/pubmed/29773645>
- 1051 23. Ragni C V., Diguët N, Le Garrec J-F, Novotova M, Resende TP, Pop S, et al. Amotl1
1052 mediates sequestration of the Hippo effector Yap1 downstream of Fat4 to restrict heart
1053 growth. *Nat Commun* [Internet]. 2017 Feb 27 [cited 2018 Sep 6];8:14582. Available
1054 from: <http://www.ncbi.nlm.nih.gov/pubmed/28239148>
- 1055 24. Leach JP, Heallen T, Zhang M, Rahmani M, Morikawa Y, Hill MC, et al. Hippo
1056 pathway deficiency reverses systolic heart failure after infarction. *Nature* [Internet].

- 1057 2017 Oct 4 [cited 2018 Sep 6];550(7675):260–4. Available from:
1058 <http://www.ncbi.nlm.nih.gov/pubmed/28976966>
- 1059 25. Bassat E, Mutlak YE, Genzelinakh A, Shadrin IY, Baruch Umansky K, Yifa O, et al.
1060 The extracellular matrix protein agrin promotes heart regeneration in mice. Nature
1061 [Internet]. 2017 Jun 13 [cited 2018 Sep 6];547(7662):179–84. Available from:
1062 <http://www.nature.com/doi/10.1038/nature22978>
- 1063 26. Singh A, Ramesh S, Cibi DM, Yun LS, Li J, Li L, et al. Hippo Signaling Mediators
1064 Yap and Taz Are Required in the Epicardium for Coronary Vasculature Development.
1065 Cell Rep [Internet]. 2016 May 17 [cited 2018 Sep 6];15(7):1384–93. Available from:
1066 <http://www.ncbi.nlm.nih.gov/pubmed/27160901>
- 1067 27. Elosegui-Artola A, Andreu I, Beedle AEM, Lezamiz A, Uroz M, Kosmalska AJ, et al.
1068 Force Triggers YAP Nuclear Entry by Regulating Transport across Nuclear Pores. Cell
1069 [Internet]. 2017 Nov 30 [cited 2018 Sep 6];171(6):1397-1410.e14. Available from:
1070 <http://www.ncbi.nlm.nih.gov/pubmed/29107331>
- 1071 28. Bratt A, Wilson WJ, Troyanovsky B, Aase K, Kessler R, Van Meir EG, et al.
1072 Angiotensin belongs to a novel protein family with conserved coiled-coil and PDZ
1073 binding domains. Gene [Internet]. 2002 Sep 18 [cited 2018 Sep 6];298(1):69–77.
1074 Available from: <http://www.ncbi.nlm.nih.gov/pubmed/12406577>
- 1075 29. Zheng Y, Vertuani S, Nyström S, Audebert S, Meijer I, Tegnebratt T, et al.
1076 Angiotensin-like protein 1 controls endothelial polarity and junction stability during
1077 sprouting angiogenesis. Circ Res [Internet]. 2009 Jul 31 [cited 2018 Sep
1078 6];105(3):260–70. Available from:
1079 <http://circres.ahajournals.org/cgi/doi/10.1161/CIRCRESAHA.109.195156>
- 1080 30. DeRan M, Yang J, Shen C-H, Peters EC, Fitamant J, Chan P, et al. Energy Stress
1081 Regulates Hippo-YAP Signaling Involving AMPK-Mediated Regulation of

- 1082 Angiotensin-like 1 Protein. Cell Rep [Internet]. 2014 Oct 23 [cited 2018 Sep
1083 6];9(2):495–503. Available from: <http://www.ncbi.nlm.nih.gov/pubmed/25373897>
- 1084 31. Zhao B, Li L, Lu Q, Wang LH, Liu C-Y, Lei Q, et al. Angiotensin is a novel Hippo
1085 pathway component that inhibits YAP oncoprotein. Genes Dev [Internet]. 2011 Jan 1
1086 [cited 2018 Sep 6];25(1):51–63. Available from:
1087 <http://www.ncbi.nlm.nih.gov/pubmed/21205866>
- 1088 32. Wang W, Huang J, Chen J. Angiotensin-like Proteins Associate with and Negatively
1089 Regulate YAP1. J Biol Chem [Internet]. 2011 Feb 11 [cited 2018 Sep 6];286(6):4364–
1090 70. Available from: <http://www.ncbi.nlm.nih.gov/pubmed/21187284>
- 1091 33. Agarwala S, Duquesne S, Liu K, Boehm A, Grimm L, Link S, et al. Amotl2a interacts
1092 with the Hippo effector Yap1 and the Wnt/ β -catenin effector Lef1 to control tissue size
1093 in zebrafish. Elife [Internet]. 2015 Sep 3 [cited 2018 Sep 6];4:e08201. Available from:
1094 <http://www.ncbi.nlm.nih.gov/pubmed/26335201>
- 1095 34. Nakajima H, Yamamoto K, Agarwala S, Terai K, Fukui H, Fukuhara S, et al. Flow-
1096 Dependent Endothelial YAP Regulation Contributes to Vessel Maintenance. Dev Cell
1097 [Internet]. 2017 Mar 27 [cited 2018 Sep 6];40(6):523-536.e6. Available from:
1098 <http://www.ncbi.nlm.nih.gov/pubmed/28350986>
- 1099 35. Habbig S, Bartram MP, Sägmüller JG, Griessmann A, Franke M, Müller R-U, et al.
1100 The ciliopathy disease protein NPHP9 promotes nuclear delivery and activation of the
1101 oncogenic transcriptional regulator TAZ. Hum Mol Genet [Internet]. 2012 Dec 15
1102 [cited 2018 Sep 6];21(26):5528–38. Available from:
1103 <http://www.ncbi.nlm.nih.gov/pubmed/23026745>
- 1104 36. Frank V, Habbig S, Bartram MP, Eisenberger T, Veenstra-Knol HE, Decker C, et al.
1105 Mutations in NEK8 link multiple organ dysplasia with altered Hippo signalling and
1106 increased c-MYC expression. Hum Mol Genet [Internet]. 2013 Jun 1 [cited 2018 Sep

- 6];22(11):2177–85. Available from: <http://www.ncbi.nlm.nih.gov/pubmed/23418306>
37. Grampa V, Delous M, Zaidan M, Ody G, Thomas S, Elkhartoufi N, et al. Novel NEK8 Mutations Cause Severe Syndromic Renal Cystic Dysplasia through YAP Dysregulation. Beier DR, editor. PLOS Genet [Internet]. 2016 Mar 11 [cited 2018 Sep 6];12(3):e1005894. Available from: <http://www.ncbi.nlm.nih.gov/pubmed/26967905>
38. Kim M, Kim M, Lee M-S, Kim C-H, Lim D-S. The MST1/2-SAV1 complex of the Hippo pathway promotes ciliogenesis. Nat Commun [Internet]. 2014 Dec 4 [cited 2018 Sep 6];5(1):5370. Available from: <http://www.ncbi.nlm.nih.gov/pubmed/25367221>
39. Männer J, Schlueter J, Brand T. Experimental analyses of the function of the proepicardium using a new microsurgical procedure to induce loss-of-proepicardial-function in chick embryos. Dev Dyn [Internet]. 2005 Aug [cited 2018 Sep 6];233(4):1454–63. Available from: <http://www.ncbi.nlm.nih.gov/pubmed/15977171>
40. Moore AW, McInnes L, Kreidberg J, Hastie ND, Schedl A. YAC complementation shows a requirement for Wt1 in the development of epicardium, adrenal gland and throughout nephrogenesis. Development [Internet]. 1999 May [cited 2018 Sep 6];126(9):1845–57. Available from: <http://www.ncbi.nlm.nih.gov/pubmed/10101119>
41. Wu S-P, Dong X-R, Regan JN, Su C, Majesky MW. Tbx18 regulates development of the epicardium and coronary vessels. Dev Biol [Internet]. 2013 Nov 15 [cited 2018 Sep 6];383(2):307–20. Available from: <http://www.ncbi.nlm.nih.gov/pubmed/24016759>
42. González-Rosa JM, Peralta M, Mercader N. Pan-epicardial lineage tracing reveals that epicardium derived cells give rise to myofibroblasts and perivascular cells during zebrafish heart regeneration. Dev Biol [Internet]. 2012 Oct 15 [cited 2018 Sep 6];370(2):173–86. Available from: <http://www.ncbi.nlm.nih.gov/pubmed/22877945>
43. Kikuchi K, Poss KD. Cardiac Regenerative Capacity and Mechanisms. Annu Rev Cell Dev Biol [Internet]. 2012 Nov 10 [cited 2018 Sep 6];28(1):719–41. Available from:

- 1132 <http://www.ncbi.nlm.nih.gov/pubmed/23057748>
- 1133 44. Limana F, Capogrossi MC, Germani A. The epicardium in cardiac repair: From the
1134 stem cell view. *Pharmacol Ther* [Internet]. 2011 Jan [cited 2018 Sep 6];129(1):82–96.
1135 Available from: <http://www.ncbi.nlm.nih.gov/pubmed/20937304>
- 1136 45. Katz TC, Singh MK, Degenhardt K, Rivera-Feliciano J, Johnson RL, Epstein JA, et al.
1137 Distinct Compartments of the Proepicardial Organ Give Rise to Coronary Vascular
1138 Endothelial Cells. *Dev Cell* [Internet]. 2012 Mar 13 [cited 2018 Sep 6];22(3):639–50.
1139 Available from: <http://www.ncbi.nlm.nih.gov/pubmed/22421048>
- 1140 46. Peralta M, Steed E, Harlepp S, González-Rosa JM, Monduc F, Ariza-Cosano A, et al.
1141 Heartbeat-driven pericardiac fluid forces contribute to epicardium morphogenesis. *Curr*
1142 *Biol* [Internet]. 2013 Sep 23 [cited 2018 Sep 6];23(18):1726–35. Available from:
1143 <http://linkinghub.elsevier.com/retrieve/pii/S0960982213008282>
- 1144 47. Mikawa T, Fischman DA. Retroviral analysis of cardiac morphogenesis: discontinuous
1145 formation of coronary vessels. *Proc Natl Acad Sci U S A* [Internet]. 1992 Oct 15 [cited
1146 2018 Sep 6];89(20):9504–8. Available from:
1147 <http://www.ncbi.nlm.nih.gov/pubmed/1409660>
- 1148 48. Mikawa T, Gourdie RG. Pericardial Mesoderm Generates a Population of Coronary
1149 Smooth Muscle Cells Migrating into the Heart along with Ingrowth of the Epicardial
1150 Organ. *Dev Biol* [Internet]. 1996 Mar 15 [cited 2018 Sep 6];174(2):221–32. Available
1151 from: <http://www.ncbi.nlm.nih.gov/pubmed/8631495>
- 1152 49. Acharya A, Baek ST, Huang G, Eskiocak B, Goetsch S, Sung CY, et al. The bHLH
1153 transcription factor Tcf21 is required for lineage-specific EMT of cardiac fibroblast
1154 progenitors. *Development* [Internet]. 2012 Jun 15 [cited 2018 Sep 6];139(12):2139–49.
1155 Available from: <http://dev.biologists.org/cgi/doi/10.1242/dev.079970>
- 1156 50. Liu J, Stainier DYR. Tbx5 and Bmp Signaling Are Essential for Proepicardium

- 1157 Specification in Zebrafish. *Circ Res* [Internet]. 2010 Jun 25 [cited 2018 Sep
1158 6];106(12):1818–28. Available from: <http://www.ncbi.nlm.nih.gov/pubmed/20413782>
- 1159 51. Ishii Y, Garriock RJ, Navetta AM, Coughlin LE, Mikawa T. BMP Signals Promote
1160 Proepicardial Protrusion Necessary for Recruitment of Coronary Vessel and Epicardial
1161 Progenitors to the Heart. *Dev Cell* [Internet]. 2010 Aug [cited 2018 Sep 6];19(2):307–
1162 16. Available from: <http://linkinghub.elsevier.com/retrieve/pii/S153458071000345X>
- 1163 52. Schlueter J, Männer J, Brand T. BMP is an important regulator of proepicardial identity
1164 in the chick embryo. *Dev Biol* [Internet]. 2006 Jul 15 [cited 2018 Sep 6];295(2):546–
1165 58. Available from: <http://linkinghub.elsevier.com/retrieve/pii/S0012160606002405>
- 1166 53. Tsujikawa M, Malicki J. Intraflagellar transport genes are essential for differentiation
1167 and survival of vertebrate sensory neurons. *Neuron* [Internet]. 2004 Jun 10 [cited 2018
1168 Sep 6];42(5):703–16. Available from: <http://www.ncbi.nlm.nih.gov/pubmed/15182712>
- 1169 54. Tay SY, Yu X, Wong KN, Panse P, Ng CP, Roy S. The iguana/DZIP1 protein is a
1170 novel component of the ciliogenic pathway essential for axonemal biogenesis. *Dev*
1171 *Dyn* [Internet]. 2010 Feb [cited 2018 Sep 6];239(2):527–34. Available from:
1172 <http://www.ncbi.nlm.nih.gov/pubmed/20014402>
- 1173 55. Kim H, Richardson J, van Eeden F, Ingham PW. Gli2a protein localization reveals a
1174 role for Iguana/DZIP1 in primary ciliogenesis and a dependence of Hedgehog signal
1175 transduction on primary cilia in the zebrafish. *BMC Biol* [Internet]. 2010 Apr 19 [cited
1176 2018 Sep 6];8(1):65. Available from:
1177 <http://bmcbiol.biomedcentral.com/articles/10.1186/1741-7007-8-65>
- 1178 56. Borovina A, Superina S, Voskas D, Ciruna B. Vangl2 directs the posterior tilting and
1179 asymmetric localization of motile primary cilia. *Nat Cell Biol* [Internet]. 2010 Apr 21
1180 [cited 2018 Sep 6];12(4):407–12. Available from:
1181 <http://www.ncbi.nlm.nih.gov/pubmed/20305649>

- 1182 57. Sun Z, Amsterdam A, Pazour GJ, Cole DG, Miller MS, Hopkins N. A genetic screen in
1183 zebrafish identifies cilia genes as a principal cause of cystic kidney. *Development*
1184 [Internet]. 2004 Aug 15 [cited 2019 Jul 15];131(16):4085–93. Available from:
1185 <http://www.ncbi.nlm.nih.gov/pubmed/10804177>
- 1186 58. Huang P, Schier AF. Dampened Hedgehog signaling but normal Wnt signaling in
1187 zebrafish without cilia. *Development* [Internet]. 2009 Sep 15 [cited 2018 Sep
1188 6];136(18):3089–98. Available from: <http://www.ncbi.nlm.nih.gov/pubmed/19700616>
- 1189 59. Carmona R, González-Iriarte M, Pérez-Pomares JM, Muñoz-Chápuli R. Localization of
1190 the Wilm’s tumour protein WT1 in avian embryos. *Cell Tissue Res* [Internet]. 2001
1191 Feb [cited 2018 Sep 6];303(2):173–86. Available from:
1192 <http://www.ncbi.nlm.nih.gov/pubmed/11291764>
- 1193 60. Hansen CG, Moroishi T, Guan K-L. YAP and TAZ: a nexus for Hippo signaling and
1194 beyond. *Trends Cell Biol* [Internet]. 2015 Sep [cited 2018 Sep 17];25(9):499–513.
1195 Available from: <http://www.ncbi.nlm.nih.gov/pubmed/26045258>
- 1196 61. Miesfeld JB, Link BA. Establishment of transgenic lines to monitor and manipulate
1197 Yap/Taz-Tead activity in zebrafish reveals both evolutionarily conserved and divergent
1198 functions of the Hippo pathway. *Mech Dev* [Internet]. 2014 Aug [cited 2018 Sep
1199 6];133:177–88. Available from: <http://www.ncbi.nlm.nih.gov/pubmed/24560909>
- 1200 62. Liu-Chittenden Y, Huang B, Shim JS, Chen Q, Lee S-J, Anders RA, et al. Genetic and
1201 pharmacological disruption of the TEAD-YAP complex suppresses the oncogenic
1202 activity of YAP. *Genes Dev* [Internet]. 2012 Jun 15 [cited 2019 Jul 15];26(12):1300–5.
1203 Available from: <http://www.ncbi.nlm.nih.gov/pubmed/22677547>
- 1204 63. Wang W, Li N, Li X, Tran MK, Han X, Chen J. Tankyrase Inhibitors Target YAP by
1205 Stabilizing Angiomotin Family Proteins. *Cell Rep* [Internet]. 2015 Oct 20 [cited 2019
1206 Jul 15];13(3):524–32. Available from: <http://www.ncbi.nlm.nih.gov/pubmed/26456820>

- 1207 64. Lancaster MA, Schroth J, Gleeson JG. Subcellular spatial regulation of canonical Wnt
1208 signalling at the primary cilium. *Nat Cell Biol* [Internet]. 2011 Jun 22 [cited 2018 Sep
1209 13];13(6):700–7. Available from: <http://www.ncbi.nlm.nih.gov/pubmed/21602792>
- 1210 65. Cao Y, Park A, Sun Z. Intraflagellar transport proteins are essential for cilia formation
1211 and for planar cell polarity. *J Am Soc Nephrol* [Internet]. 2010 Aug 1 [cited 2018 Sep
1212 6];21(8):1326–33. Available from:
1213 <http://www.jasn.org/cgi/doi/10.1681/ASN.2009091001>
- 1214 66. Ocbina PJR, Eggenschwiler JT, Moskowitz I, Anderson K V. Complex interactions
1215 between genes controlling trafficking in primary cilia. *Nat Genet* [Internet]. 2011 Jun 8
1216 [cited 2019 Jul 30];43(6):547–53. Available from:
1217 <http://www.ncbi.nlm.nih.gov/pubmed/21552265>
- 1218 67. Zanconato F, Cordenonsi M, Piccolo S. YAP/TAZ at the Roots of Cancer. *Cancer Cell*
1219 [Internet]. 2016 Jun 13 [cited 2018 Sep 6];29(6):783–803. Available from:
1220 <http://www.ncbi.nlm.nih.gov/pubmed/27300434>
- 1221 68. Oh S-H, Swiderska-Syn M, Jewell ML, Premont RT, Diehl AM. Liver regeneration
1222 requires Yap1-TGFβ-dependent epithelial-mesenchymal transition in hepatocytes. *J*
1223 *Hepatol* [Internet]. 2018 Aug [cited 2018 Sep 6];69(2):359–67. Available from:
1224 <http://www.ncbi.nlm.nih.gov/pubmed/29758331>
- 1225 69. Artap S, Manderfield LJ, Smith CL, Poleshko A, Aghajanian H, See K, et al.
1226 Endocardial Hippo signaling regulates myocardial growth and cardiogenesis. *Dev Biol*
1227 [Internet]. 2018 Aug 1 [cited 2018 Sep 6];440(1):22–30. Available from:
1228 <http://www.ncbi.nlm.nih.gov/pubmed/29727635>
- 1229 70. Yu F-X, Zhao B, Guan K-L. Hippo Pathway in Organ Size Control, Tissue
1230 Homeostasis, and Cancer. *Cell* [Internet]. 2015 Nov 5 [cited 2018 Sep 6];163(4):811–
1231 28. Available from: <http://www.ncbi.nlm.nih.gov/pubmed/26544935>

- 1232 71. Thompson BJ, Sahai E. MST kinases in development and disease. J Cell Biol
1233 [Internet]. 2015 Sep 14 [cited 2018 Sep 6];210(6):871–82. Available from:
1234 <http://www.ncbi.nlm.nih.gov/pubmed/26370497>
- 1235 72. Sun Y, Yong KMA, Villa-Diaz LG, Zhang X, Chen W, Philson R, et al. Hippo/YAP-
1236 mediated rigidity-dependent motor neuron differentiation of human pluripotent
1237 stem cells. Nat Mater [Internet]. 2014 Jun 13 [cited 2018 Sep 6];13(6):599–604.
1238 Available from: <http://www.ncbi.nlm.nih.gov/pubmed/24728461>
- 1239 73. Yi C, Shen Z, Stemmer-Rachamimov A, Dawany N, Troutman S, Showe LC, et al. The
1240 p130 Isoform of Angiomotin Is Required for Yap-Mediated Hepatic Epithelial Cell
1241 Proliferation and Tumorigenesis. Sci Signal [Internet]. 2013 Sep 3 [cited 2018 Sep
1242 6];6(291):ra77–ra77. Available from: <http://www.ncbi.nlm.nih.gov/pubmed/24003254>
- 1243 74. Piccolo S, Dupont S, Cordenonsi M. The Biology of YAP/TAZ: Hippo Signaling and
1244 Beyond. Physiol Rev [Internet]. 2014 Oct [cited 2019 Jul 30];94(4):1287–312.
1245 Available from: <http://www.ncbi.nlm.nih.gov/pubmed/25287865>
- 1246 75. Vuong LT, Iomini C, Balmer S, Esposito D, Aaronson SA, Mlodzik M. Kinesin-2 and
1247 IFT-A act as a complex promoting nuclear localization of β -catenin during Wnt
1248 signalling. Nat Commun [Internet]. 2018 Dec 13 [cited 2019 Jul 18];9(1):5304.
1249 Available from: <http://www.nature.com/articles/s41467-018-07605-z>
- 1250 76. Behal RH, Miller MS, Qin H, Lucker BF, Jones A, Cole DG. Subunit Interactions and
1251 Organization of the *Chlamydomonas reinhardtii* Intraflagellar Transport Complex A
1252 Proteins. J Biol Chem [Internet]. 2012 Apr 6 [cited 2019 Jul 30];287(15):11689–703.
1253 Available from: <http://www.ncbi.nlm.nih.gov/pubmed/22170070>
- 1254 77. Piperno G, Siuda E, Henderson S, Segil M, Vaananen H, Sassaroli M. Distinct mutants
1255 of retrograde intraflagellar transport (IFT) share similar morphological and molecular
1256 defects. J Cell Biol [Internet]. 1998 Dec 14 [cited 2019 Jul 30];143(6):1591–601.

- 1257 Available from: <http://www.ncbi.nlm.nih.gov/pubmed/9852153>
- 1258 78. Iomini C, Li L, Esparza JM, Dutcher SK. Retrograde Intraflagellar Transport Mutants
1259 Identify Complex A Proteins With Multiple Genetic Interactions in *Chlamydomonas*
1260 *reinhardtii*. Genetics [Internet]. 2009 Nov [cited 2019 Jul 30];183(3):885–96.
1261 Available from: <http://www.ncbi.nlm.nih.gov/pubmed/19720863>
- 1262 79. Rudat C, Norden J, Taketo MM, Kispert A. Epicardial function of canonical Wnt-,
1263 Hedgehog-, Fgfr1/2-, and Pdgfra-signalling. Cardiovasc Res [Internet]. 2013 Dec 1
1264 [cited 2019 Jul 18];100(3):411–21. Available from:
1265 <https://academic.oup.com/cardiovasres/article-lookup/doi/10.1093/cvr/cvt210>
- 1266 80. Sugimoto K, Hui SP, Sheng DZ, Kikuchi K. Dissection of zebrafish shha function
1267 using site-specific targeting with a Cre-dependent genetic switch. Elife [Internet]. 2017
1268 May 17 [cited 2019 Jul 18];6. Available from:
1269 <http://www.ncbi.nlm.nih.gov/pubmed/28513431>
- 1270 81. Robb L, Mifsud L, Hartley L, Biben C, Copeland NG, Gilbert DJ, et al. epicardin: A
1271 novel basic helix-loop-helix transcription factor gene expressed in epicardium,
1272 branchial arch myoblasts, and mesenchyme of developing lung, gut, kidney, and
1273 gonads. Dev Dyn [Internet]. 1998 Sep [cited 2019 Jul 18];213(1):105–13. Available
1274 from: [http://doi.wiley.com/10.1002/%28SICI%291097-](http://doi.wiley.com/10.1002/%28SICI%291097-0177%28199809%29213%3A1%3C105%3A%3AAID-AJA10%3E3.0.CO%3B2-1)
1275 [0177%28199809%29213%3A1%3C105%3A%3AAID-AJA10%3E3.0.CO%3B2-1](http://doi.wiley.com/10.1002/%28SICI%291097-0177%28199809%29213%3A1%3C105%3A%3AAID-AJA10%3E3.0.CO%3B2-1)
- 1276 82. Andrés-Delgado L, Ernst A, Galardi-Castilla M, Bazaga D, Peralta M, Münch J, et al.
1277 Actin dynamics and the Bmp pathway drive apical extrusion of proepicardial cells.
1278 Development [Internet]. 2019 Jul 1 [cited 2019 Jul 18];146(13):dev174961. Available
1279 from: <http://www.ncbi.nlm.nih.gov/pubmed/31175121>
- 1280 83. Villalobos E, Criollo A, Schiattarella GG, Altamirano F, French KM, May HI, et al.
1281 Fibroblast Primary Cilia Are Required for Cardiac Fibrosis. Circulation [Internet].

- 1282 2019 May 14 [cited 2019 Jul 30];139(20):2342–57. Available from:
1283 <https://www.ahajournals.org/doi/10.1161/CIRCULATIONAHA.117.028752>
- 1284 84. Mönnich M, Borgeskov L, Breslin L, Jakobsen L, Rogowski M, Doganli C, et al.
1285 CEP128 Localizes to the Subdistal Appendages of the Mother Centriole and Regulates
1286 TGF- β /BMP Signaling at the Primary Cilium. *Cell Rep* [Internet]. 2018 Mar [cited
1287 2019 Jul 30];22(10):2584–92. Available from:
1288 <https://linkinghub.elsevier.com/retrieve/pii/S2211124718302249>
- 1289 85. Vion A-C, Alt S, Klaus-Bergmann A, Szymborska A, Zheng T, Perovic T, et al.
1290 Primary cilia sensitize endothelial cells to BMP and prevent excessive vascular
1291 regression. *J Cell Biol* [Internet]. 2018 May 7 [cited 2018 Sep 6];217(5):1651–65.
1292 Available from: <http://www.ncbi.nlm.nih.gov/pubmed/29500191>
- 1293 86. Simões FC, Riley PR. The ontogeny, activation and function of the epicardium during
1294 heart development and regeneration. *Development* [Internet]. 2018 Apr 1 [cited 2019
1295 Jul 30];145(7):dev155994. Available from:
1296 <http://www.ncbi.nlm.nih.gov/pubmed/29592950>
- 1297 87. Kikuchi K, Gupta V, Wang J, Holdway JE, Wills AA, Fang Y, et al. tcf21+ epicardial
1298 cells adopt non-myocardial fates during zebrafish heart development and regeneration.
1299 *Development*. 2011 Jul 15;138(14):2895–902.
- 1300 88. Jonassen JA, San Agustin J, Follit JA, Pazour GJ. Deletion of IFT20 in the mouse
1301 kidney causes misorientation of the mitotic spindle and cystic kidney disease. *J Cell*
1302 *Biol* [Internet]. 2008 Nov 3 [cited 2018 Sep 6];183(3):377–84. Available from:
1303 <http://www.ncbi.nlm.nih.gov/pubmed/18981227>
- 1304 89. Haycraft CJ, Zhang Q, Song B, Jackson WS, Detloff PJ, Serra R, et al. Intraflagellar
1305 transport is essential for endochondral bone formation. *Development* [Internet]. 2007
1306 Jan 15 [cited 2018 Sep 6];134(2):307–16. Available from:

- 1307 <http://dev.biologists.org/cgi/doi/10.1242/dev.02732>
- 1308 90. Holland AJ, Fachinetti D, Han JS, Cleveland DW. Inducible, reversible system for the
- 1309 rapid and complete degradation of proteins in mammalian cells. *Proc Natl Acad Sci*
- 1310 [Internet]. 2012 Dec 4 [cited 2018 Sep 14];109(49):E3350–7. Available from:
- 1311 <http://www.ncbi.nlm.nih.gov/pubmed/23150568>
- 1312 91. Cong L, Ran FA, Cox D, Lin S, Barretto R, Habib N, et al. Multiplex genome
- 1313 engineering using CRISPR/Cas systems. *Science* [Internet]. 2013 Feb 15 [cited 2018
- 1314 Sep 14];339(6121):819–23. Available from:
- 1315 <http://www.ncbi.nlm.nih.gov/pubmed/23287718>
- 1316 92. Pei Z, Bai Y, Schmitt AP. PIV5 M protein interaction with host protein angiomin-1
- 1317 like 1. *Virology* [Internet]. 2010 Feb 5 [cited 2018 Sep 6];397(1):155–66. Available
- 1318 from: <http://linkinghub.elsevier.com/retrieve/pii/S0042682209006941>
- 1319 93. Boin A, Couvelard A, Couderc C, Brito I, Filipescu D, Kalamirides M, et al. Proteomic
- 1320 screening identifies a YAP-driven signaling network linked to tumor cell proliferation
- 1321 in human schwannomas. *Neuro Oncol* [Internet]. 2014 Sep [cited 2018 Sep
- 1322 6];16(9):1196–209. Available from: [https://academic.oup.com/neuro-oncology/article-](https://academic.oup.com/neuro-oncology/article-lookup/doi/10.1093/neuonc/nou020)
- 1323 [lookup/doi/10.1093/neuonc/nou020](https://academic.oup.com/neuro-oncology/article-lookup/doi/10.1093/neuonc/nou020)
- 1324 94. He M, Subramanian R, Bangs F, Omelchenko T, Liem Jr KF, Kapoor TM, et al. The
- 1325 kinesin-4 protein Kif7 regulates mammalian Hedgehog signalling by organizing the
- 1326 cilium tip compartment. *Nat Cell Biol* [Internet]. 2014 Jul 22 [cited 2018 Sep
- 1327 6];16(7):663–72. Available from: <http://www.ncbi.nlm.nih.gov/pubmed/24952464>
- 1328